Topological Rigidity and Non-Abelian Defect Junctions in Chiral Nematic Systems with Effective Biaxial Symmetry

Jin-Sheng Wu
Department of Physics and Chemical Physics Program, University of Colorado, Boulder, Colorado, USA

Roberto Abril Valenzuela
Department of Physics, University of California, Santa Barbara, California, USA

Mark J. Bowick[*]
Kavli Institute for Theoretical Physics, University of California Santa Barbara, Santa Barbara, California, USA,
French American Center for Theoretical Science, CNRS, KITP, Santa Barbara, California, USA,
and International Institute for Sustainability with Knotted Chiral Meta Matter (WPI-SKCM2), Hiroshima University, Hiroshima, Japan

Ivan I. Smalyukh[†]
Department of Physics and Chemical Physics Program, University of Colorado, Boulder, Colorado, USA,
International Institute for Sustainability with Knotted Chiral Meta Matter (WPI-SKCM2), Hiroshima University, Hiroshima, Japan,
Department of Electrical, Computer, and Energy Engineering, Materials Science and Engineering Program and Soft Materials Research Center, University of Colorado, Boulder, Colorado, USA,
and Renewable and Sustainable Energy Institute, National Renewable Energy Laboratory and University of Colorado, Boulder, Colorado, USA

(Received 5 November 2024; revised 21 February 2025; accepted 7 April 2025; published 1 May 2025)

We study topologically stable defect structures in systems where the defect line classification in three dimensions and associated algebra of interactions (the fundamental group) are governed by the non-Abelian eight-element group, the quaternions Q_8. The non-Abelian character of the defect algebra leads to a topological rigidity of bound defect pairs, and trivalent junctions which are the building blocks of multijunction trivalent networks. We realize such structures in laboratory chiral nematics and analyze their behavior analytically, along with numerical modeling.

DOI: 10.1103/PhysRevX.15.021036 Subject Areas: Condensed Matter Physics

I. INTRODUCTION

Topological defects of various intrinsic dimensions, from superfluid filaments to the atmospheric polar vortex, play important roles in a wide variety of physical systems [1–5]. Dislocation motion and entanglement are key determinants of the mechanical response of solids to applied stresses, and superconducting vortices, pinned or unpinned, are a critical source of dissipation in superconductors. Topological defects are also essential singularities in the sense that, provided topology allows them, they inevitably form in finite-rate continuous phase transitions due to critical slowing-down and, being the slowest degrees of freedom, they control the rate of such transitions [6–8]. They are distinctive fingerprints of phase transitions involving spontaneously broken symmetries in that the specific topological classes they form often distinguish different symmetry-breaking patterns and the associated order-parameter spaces.

In most cases, and especially in three dimensions, the pure interactions of the minimal-energy defects are governed by an Abelian (commutative) symmetry structure such as a discrete $\mathbb{Z}_n$ or the group of integers $\mathbb{Z}$ [1,5]. These minimal-energy defects interact only at a distance, or indirectly through their coupling to other material fields [2]. Defects then have only energetic barriers to crossing and do not form stable defect junctions or networks in the absence of pinning centers. This is the case for superfluid filaments,

[*]Contact author: bowick@kitp.ucsb.edu
[†]Contact author: ivan.smalyukh@colorado.edu

superconducting flux lines, and uniaxial three-dimensional liquid crystals (nematics), as well as elastic disclinations and dislocations.

Both biaxial liquid crystals and liquid crystals with intrinsic twist (chiral nematics) have a rich class of topological line defects that are, instead, governed by a non-Abelian (noncommutative) algebraic structure, leading to junctions where three defects meet, the physical entanglement of defects and history-dependent interactions. Here we show that all these features can be experimentally realized in a laboratory chiral nematic and agree well with theoretical predictions and the results of numerical simulations.

We experimentally visualize and demonstrate that a conventional chiral nematic displays all the key topological features expected from the non-Abelian algebra of its associated defects, including two distinct types of trivalent junctions, topological entanglement of defect pairs and stable parallel defect lines.

After introducing the key background material in Secs. II–V [1–5] and following the methods of Sec. VI, we exhibit the two basic types of trivalent defect junctions: three distinct defects meeting at a point or two defects from the same class producing or annihilating a nontrivial radial defect—the so-called -1 defect. The -1 defect is also necessarily generated when two braided defects of the same class fixed at their ends are pulled across each other, thus providing a topological obstruction to disentanglement, or said differently, generating topological rigidity for a braided pair. Such a pair is then a fundamental excitation in the system, analogous to a topologically protected and therefore stable bound state [1–5].

We then show that trivalent junctions can be joined to create an extended flexible and stable trivalent network, a filamentous and fluid fishnet, paving the way for creating a wide variety of larger-scale networks. By experimentally patterning defects of a fixed class at the surface of the experimental cell, we show that disclination lines can form handles connecting the surface to itself and bridges connecting one surface to another, all controlled by the relative sign of the topological class of the surface defects.

Finally, we analytically demonstrate the robustness of the biaxiality in chiral nematics, including the estimation of biaxial elasticities and the energetics of two parallel disclination lines where intrinsic defect repulsion is balanced by the need to minimize the energy in the twist of the chiral nematic, again leading to a stable bound state observed in our experiments.

From a broader perspective, our results apply to all three-dimensional, rotationally symmetric liquid-crystal systems with an isotropy given by the dihedral group (D_2). This occurs whenever there is a well-defined orthorhombic frame, either local or global. The global case arises in biaxial nematic liquid crystals formed from bricklike building blocks [9–15], while the emergent local counterpart case occurs in chiral nematics (cholesterics) and in hybrid molecular or colloidal systems, where the symmetry breaking in molecular and colloidal order relies crucially on the presence of a helical axis [10,15–18]. For clarity of notation, we will call the entire class D2CLC (order-two dihedral chiral liquid crystals).

D2CLC systems can be realized experimentally by exploiting the biaxiality of a chiral liquid crystal (CLC), as implemented here, or in hybrid molecular-colloidal systems (colloidal elements in a liquid-crystal environment) [10–14,17,18]. The associated topological defects are at least partially classified by the homotopy classes of the order-parameter manifold, which specifies the space of inequivalent ground states. For D2CLC, the first homotopy group of the space of ground states, known as the fundamental group, is the non-Abelian eight-element group, the quaternions Q_8 [19] first introduced by Hamilton in 1843 in an attempt to find a three-dimensional version of the complex plane [1,2]. The quaternionic fundamental group leads to five classes (conjugacy classes) of topologically stable line defects in three dimensions, one trivial class (the identity), and four nontrivial classes. The quaternionic algebra has several important consequences. Braids of two defects from distinct classes are topologically entangled [1,20,21] and can be disentangled only by creating a third distinct bridging defect. Perhaps more importantly, there are stable trivalent junctions where three defects meet, allowing the spontaneous formation of extended line-defect networks consisting of nodes (junctions) of coordination number (degree) 3 [20].

While quantum entanglement and braiding of anyons in hard condensed matter systems with topological order in two spatial dimensions is very rich [22–24], we explore here a different mechanism for physical entanglement and braiding in three spatial dimensions based solely on the nontrivial topology of the ground-state manifold.

II. BIAXIAL MODELS OF CHIRAL NEMATICS

Chiral liquid crystals are nematic systems with broken mirror symmetry, which manifests itself as helicoidal twist configurations in the apolar nematic director $\boldsymbol{\lambda}(\mathbf{r}) = -\boldsymbol{\lambda}(\mathbf{r})$. Locally, the twist defines a helical twist axis $\boldsymbol{\chi} = -\boldsymbol{\chi}$, orthogonal to $\boldsymbol{\lambda}$, providing a length scale $p/2$ over which $\boldsymbol{\lambda}$ rotates by π, forming one cholesteric quasilayer [Fig. 1(a)]. The local set of fields $(\boldsymbol{\lambda}, \boldsymbol{\chi}, \boldsymbol{\tau})$ derived from the twist defines the molecular field, helical axis field, and a third orthogonal direction ($\boldsymbol{\tau} = \boldsymbol{\lambda} \times \boldsymbol{\chi}$), respectively [see Fig. 1(a)]. This establishes a local triad of orthogonal directors and leads to a connection between CLCs and orthorhombic biaxial systems described by three mutually orthogonal fields $(\mathbf{n}, \mathbf{m}, \mathbf{l})$. Conceptually, the nondegeneracy of $(\boldsymbol{\lambda}, \boldsymbol{\chi}, \boldsymbol{\tau})$ (and most importantly, the latter two) already breaks uniaxial symmetry because of the intrinsic biaxial features of twist alignment. Physically, the orientational distributions of molecular orientations relative to

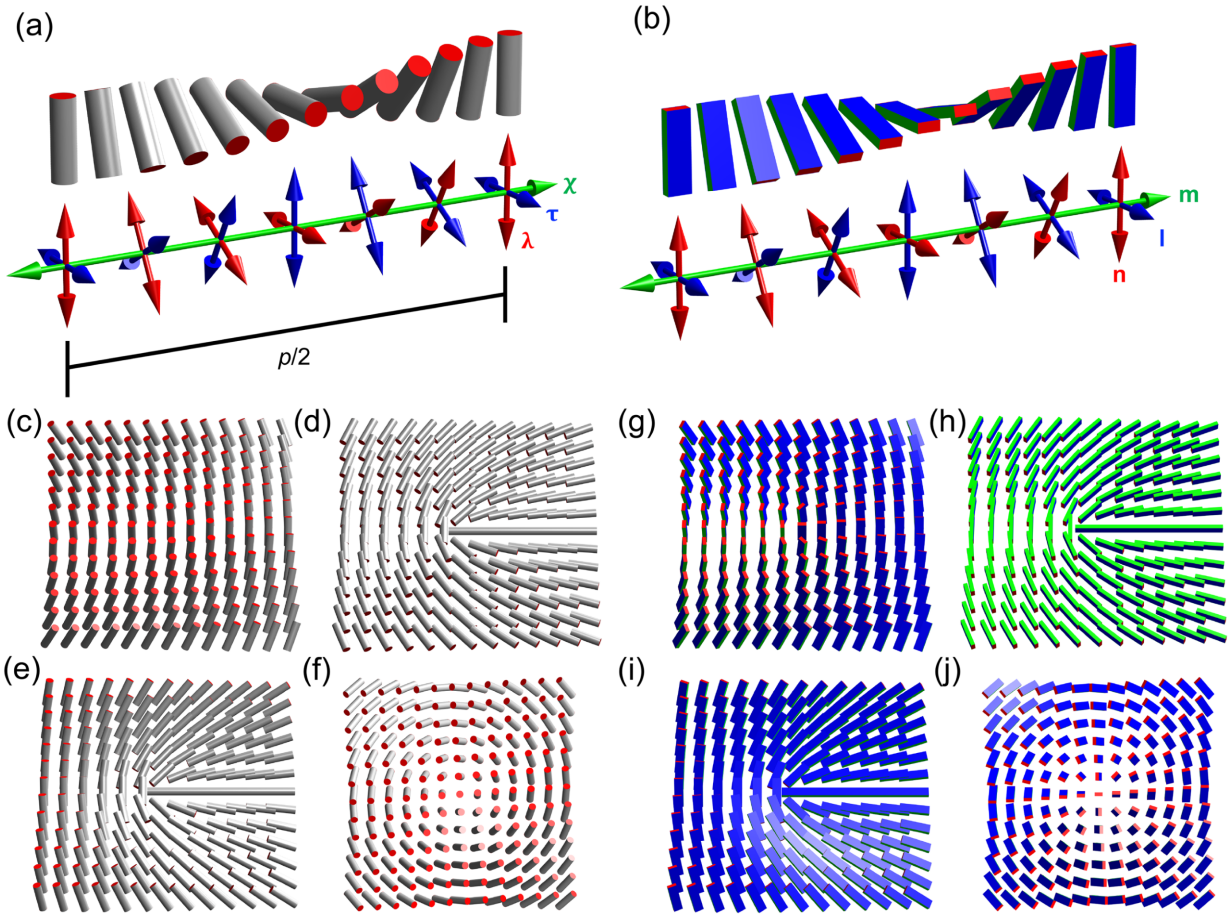

FIG. 1. (a),(b) Field definition in the (a) chiral nematic setting and (b) respective biaxial fields under the mapping established in Sec. II. The cholesteric pitch p is defined as the distance for a nematic constituent director $\boldsymbol{\lambda}$ to rotate by 2π along helical axis $\boldsymbol{\chi}$ as shown in (a). The corresponding fields describing biaxiality $(\mathbf{n},\mathbf{m},\mathbf{l})$ define the biaxial triad parallel to brick edges in (b). (c)–(f) Cross sections of line-defect textures in chiral nematics belonging to C_λ, C_χ, C_τ, and -1 defect classes, respectively. (g)–(j) Corresponding biaxial "brick" textures showing defects are nonsingular in $\mathbf{n}$, $\mathbf{m}$, $\mathbf{l}$, and $\mathbf{n}$, respectively, while being singular in the two other fields orthogonal to them. Here we show only one of the three representatives of the -1 defect class.

$\boldsymbol{\chi}$ and $\boldsymbol{\tau}$ are different [16,18]. To see the actual mapping between chiral and biaxial nematics, however, one needs to examine the free-energy models of CLCs from the perspective of biaxial nematics. First, it is straightforward that the molecular orientation is identical to the nematic director $\boldsymbol{\lambda} \equiv \mathbf{n}$. The remaining mapping from the chiral nematic frame $(\boldsymbol{\lambda},\boldsymbol{\chi},\boldsymbol{\tau})$ to the biaxial frame $(\mathbf{n},\mathbf{m},\mathbf{l})$ is revealed by the tensorial model of CLC free energies detailed below.

In the tensorial model, the orientational order in a CLC is encoded in the traceless, symmetric tensor order parameter Q_{ij} given in terms of the directors $\mathbf{n}$ and $\mathbf{m}$ by

$$Q_{ij} = S\left(n_i n_j - \frac{\delta_{ij}}{3}\right) + T\left(m_i m_j - \frac{\delta_{ij}}{3}\right), \tag{1}$$

where S and T are the uniaxial and biaxial orientational order parameters, respectively, and δ_{ij} is the Kronecker delta. One may write the strain-free elastic free-energy density as a sum of derivatives of Q_{ij} [25–27]:

$$f_{\text{elastic}} = \gamma_1 \partial_k Q_{ij} \partial_k Q_{ij} + \gamma_2 \partial_j Q_{ij} \partial_k Q_{ik} + \gamma_6 Q_{ij} \partial_i Q_{kl} \partial_j Q_{kl}. \tag{2}$$

Another second-order term $\gamma_3 \partial_k Q_{ij} \partial_j Q_{ik}$ is sometimes considered in the tensorial model. In our analysis of the bulk elastic energies, however, γ_3 differs from γ_2 only by a surface integral and so this term is dropped [25]. A third-order term is also necessary to incorporate anisotropy of the elastic contributions [28,29]. Chirality may be introduced, to lowest order, by adding a term of the form

$$f_{\text{chiral}} = \gamma_4 \epsilon_{ijk} Q_{il} \partial_j Q_{kl}, \tag{3}$$

where ϵ_{ijk} is the Levi-Civita tensor [29].

The diagonalization of the $\mathbf{Q}$ tensor sets the orthonormal triad $(\mathbf{n},\mathbf{m},\mathbf{l})$, as in Eq. (1) (see Sec. VI). On the other hand, by identifying the molecular axes and the principal director $\boldsymbol{\lambda} \equiv \mathbf{n}$, one can also reconstruct the chiral directors

$(\boldsymbol{\lambda},\boldsymbol{\chi},\boldsymbol{\tau})$ based on methods connected to the twist in $\mathbf{n}$ [30–32]. For a variety of CLC structures derived from minimizing the free energy Eqs. (2) and (3), we find that the helical axis $\boldsymbol{\chi}$, along which $\boldsymbol{\lambda}$ rotates, is consistently aligned with the direction of the biaxial director $\boldsymbol{\chi} \equiv \mathbf{m}$ (Fig. 1). In our CLC systems then, where twist is the dominant elastic deformation, the biaxiality comes mainly from minimizing the chiral term Eq. (3). Lastly, the transverse molecular axis is the cross product of the other two directors and represents the third axis $\boldsymbol{\tau} \equiv \mathbf{l}$, and the mapping of chiral nematic directors to orthorhombic biaxial directors is valid for CLC systems with a consistent twisting handedness.

Figures 1(a) and 1(b) show a comparison of the chiral and biaxial field definitions indicating the direct mapping of the molecular and helical axes. In a variety of structures, such as elementary defects in Figs. 1(c)–1(j), we can see how the twisting alignment of the molecular director $\boldsymbol{\lambda}$ determines the orientation of the corresponding biaxial directors. Furthermore, the degree of biaxiality $T \propto q^2$, with chirality $q = 2\pi/p$ the principal eigenvalue of the handedness tensor [16,17], suggesting an interchangeable interpretation of biaxiality and chirality in CLCs based on their symmetries. In all, this leads to a biaxial structure coupled to that of the helical configuration of the D2CLC [16,18]. In fact, any deformation (not just twist) in the material director field $\boldsymbol{\lambda}$ causes weak biaxiality and, thus, the biaxial tensor field is always well defined unless the helical structure is fully unwound and the material director field is spatially uniform [33]. A biaxial frame derived from all possible deformations, for example, of the uniaxial LC director field, is discussed in Ref. [33]. The biaxial description of CLCs based on our mapping is thus more robust when applied to the analysis of defects (see Sec. VI).

III. HOMOTOPY ANALYSIS OF BIAXIAL NEMATICS

After the possibility of a biaxial phase of liquid crystals was first introduced and analyzed by Freiser [9], the topological character of the ground-state manifold (or order-parameter space) associated with symmetry breaking from an isotropic phase to a biaxial phase was analyzed by Toulouse [19]. The order-parameter space is $\mathrm{SO}(3)/D_2$, the space of all three-dimensional rotations that obey the symmetry of the rectangular box, and the resultant line defects following from its fundamental group are classified by the group of quaternions Q_8: $\pi_1[\mathrm{SO}(3)/D_2] = Q_8 = \{\pm 1, \pm i, \pm j, \pm k\}$ [21,34–36]. Unknotted ring defects were also classified in Ref. [35]. There has been much work in this area in the last 50 years (for a review, see Ref. [37]).

In contrast to uniaxial nematics, whose fundamental group algebra is Abelian (the integers in two dimensions or $\mathbb{Z}_2$ in three dimensions), the quaternions are non-Abelian. In fact, the quaternion group is the smallest non-Abelian group that arises by modding out a discrete group from the rotation group [1]. The multiplication table for the group elements of Q_8 is given in Table I. We proceed with the biaxial analogy of CLCs and relabel the quaternion elements using the fields $\boldsymbol{\lambda}, \boldsymbol{\chi}, \boldsymbol{\tau}$: $(i, j, k) \to (\lambda, \chi, \tau)$ [38].

TABLE I. Multiplication table of the quaternion group elements Q_8 using the chiral nematic fields λ, τ, χ as relabelings of the elements (i, j, k). Conjugacy class assignments are highlighted by different colors.

$\times$	1	-1	λ	$-\lambda$	τ	$-\tau$	χ	$-\chi$
1	1	-1	λ	$-\lambda$	τ	$-\tau$	χ	$-\chi$
-1	-1	1	$-\lambda$	λ	$-\tau$	τ	$-\chi$	χ
λ	λ	$-\lambda$	-1	1	χ	$-\chi$	$-\tau$	τ
$-\lambda$	$-\lambda$	λ	1	-1	$-\chi$	χ	τ	$-\tau$
τ	τ	$-\tau$	$-\chi$	χ	-1	1	λ	$-\lambda$
$-\tau$	$-\tau$	τ	χ	$-\chi$	1	-1	$-\lambda$	λ
χ	χ	$-\chi$	τ	$-\tau$	$-\lambda$	λ	-1	1
$-\chi$	$-\chi$	χ	$-\tau$	τ	λ	$-\lambda$	1	-1

A subtler consequence of having a noncommutative fundamental group is that one-dimensional defects are more properly classified by the associated conjugacy classes [1,39]. Biaxial systems have five conjugacy classes $Q_8 = \{1\} \cup \{-1\} \cup C_\lambda \cup C_\tau \cup C_\chi$ where $C_\lambda = \{\pm\lambda\}$, $C_\tau = \{\pm\tau\}$, $C_\chi = \{\pm\chi\}$. One can interpret the defect class $C_{\lambda/\tau/\chi}$ as a defect texture in which there is a singularity in all directions except the direction corresponding to $\boldsymbol{\lambda}/\boldsymbol{\tau}/\boldsymbol{\chi}$. Examples of defects of class C_χ (singular in both $\boldsymbol{\lambda}$ and $\boldsymbol{\tau}$

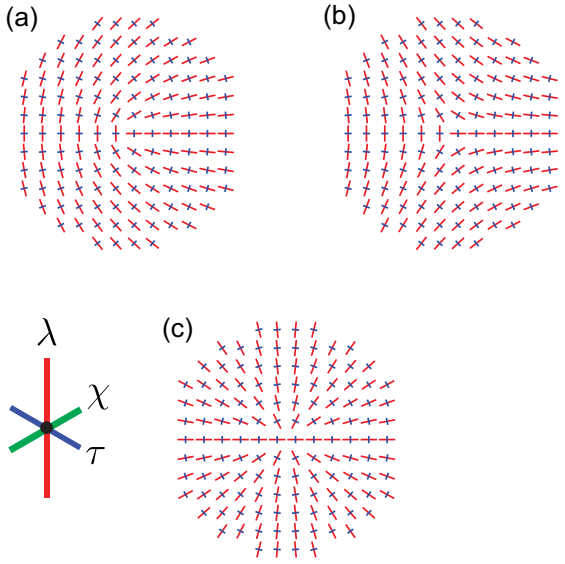

FIG. 2. (a) $+\chi$ representative of the C_χ class forming a $1/2$ disclination in both the $\boldsymbol{\lambda}$ and $\boldsymbol{\tau}$ fields and nonsingular in $\boldsymbol{\chi}$. (b) $-\chi$ representative of the C_χ class forming a $-1/2$ disclination in $\boldsymbol{\lambda}$ and $\boldsymbol{\tau}$ and nonsingular in $\boldsymbol{\chi}$ [same as Fig. 1(h)]. (c) One of the three representatives of the -1 class of defects. Note that unlike in 3D uniaxial nematics, such a defect configuration is topologically stable.

but nonsingular in χ), as well as a nonremovable -1 disclination, are shown in Figs. 1(d), 1(h), and 2 [40].

IV. GEOMETRY OF BIAXIAL AND CHIRAL NEMATIC DEFECTS

As noted, the order-parameter space spanned by the chiral triad comprised of the molecular axis λ and the helical axis χ shares the same structure as the biaxial triad and thus has the same ground-state topology [41–43]. An alternative description of chiral nematics has been recently studied experimentally in molecular-colloidal chiral hybrid systems [12,17,18]. Such systems exhibit biaxiality that depends on the colloidal concentration. It was found that, in chiral nematic hosts, biaxiality persists even at low concentrations. Moreover, the existence of a mapping from the elastic properties of chiral nematics to the biaxial free energy, described below in Sec. VIII A for conventional chiral nematics and in Ref. [44] for hybrid molecular-colloidal chiral nematics, allows one to analyze chiral nematic defects as a biaxial system. Here we treat the biaxial interpretation of CLCs as an approximation that is exact on the ground-state manifold.

V. NON-ABELIAN SIGNATURES

A. Path dependence

The loss of commutativity for a non-Abelian fundamental group of an order-parameter space has as its main consequence the loss of path independence in the composition of loops [1,38]. Mathematically, the noncommuting elements allow only one to relate two fundamental groups defined at different points up to inner automorphisms generated by a path connecting the two base points [39].

This path dependence manifests itself physically as an ambiguity in the combination of two defects; one must know the history of the paths the defects have taken to combine. As shown in Table II, the combination of two defects of the same class, say, C_τ, leads to two different results depending on the path taken. Figure 3 is an example of two such paths. In the presence of a third defect, such as C_χ, we can form two nonhomotopic curves c_1 and c_2 that are possible path histories. The path given by c_1 avoids the third defect and leads to the two defects annihilating, which is algebraically equivalent to a $+1$. The path given by c_2 is equivalent to the composition $c_1 \circ c_3$, which braids the left defect around the top defect along c_3 and then takes c_1 to combine the defects. This total path leads to a -1 defect line, meaning that the act of braiding c_3 changes the composition of the defect without changing its topological classification under the lens of the fundamental group.

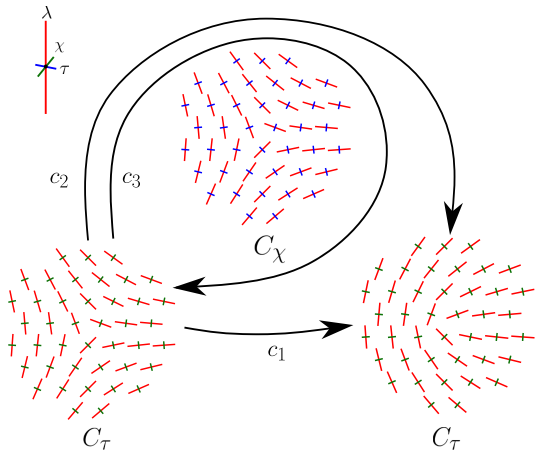

FIG. 3. Fusion of two defects belonging to the same class C_τ with the result dependent on the path taken in physical space. Path c_1 avoids other defects, resulting in the annihilation of the two C_τ defects, i.e., forming the $+1$ element. On the other hand, the path c_2 surrounds a third defect belonging to a different class, C_χ. The fusion of two C_τ defects through c_2 results in a -1 defect instead. Note that path c_2 is equivalent to compositions of c_3 and c_1.

TABLE II. Multiplication table for the conjugacy classes of Q_8. Note that combining two defects belonging to the same class produces an ambiguous result, $2(+1) \oplus 2(-1)$, where the 2 indicates the degeneracy of the result (see Table I), in which case the actual result is determined by the path taken to combine the two initial defects.

	$+1$	-1	C_λ	C_τ	C_χ
$+1$	$+1$	-1	C_λ	C_τ	C_χ
-1	$+1$	$+1$	C_λ	C_τ	C_χ
C_λ	C_λ	C_λ	$2(+1) \oplus 2(-1)$	$2C_\chi$	$2C_\tau$
C_τ	C_τ	C_τ	$2C_\chi$	$2(+1) \oplus 2(-1)$	$2C_\lambda$
C_χ	C_χ	C_χ	$2C_\tau$	$2C_\lambda$	$2(+1) \oplus 2(-1)$

B. Entanglement of defects

Arguably of more importance is the result of braiding two non-Abelian defects around each other. A loop drawn around the crossing can be deformed up to homotopy to

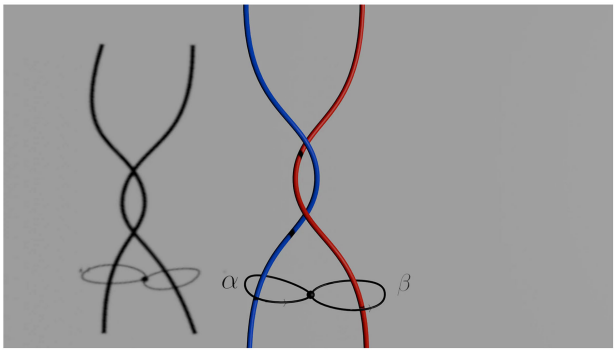

VIDEO 1. A braid of two defect lines is topologically equivalent to the commutator of the two defect classes.

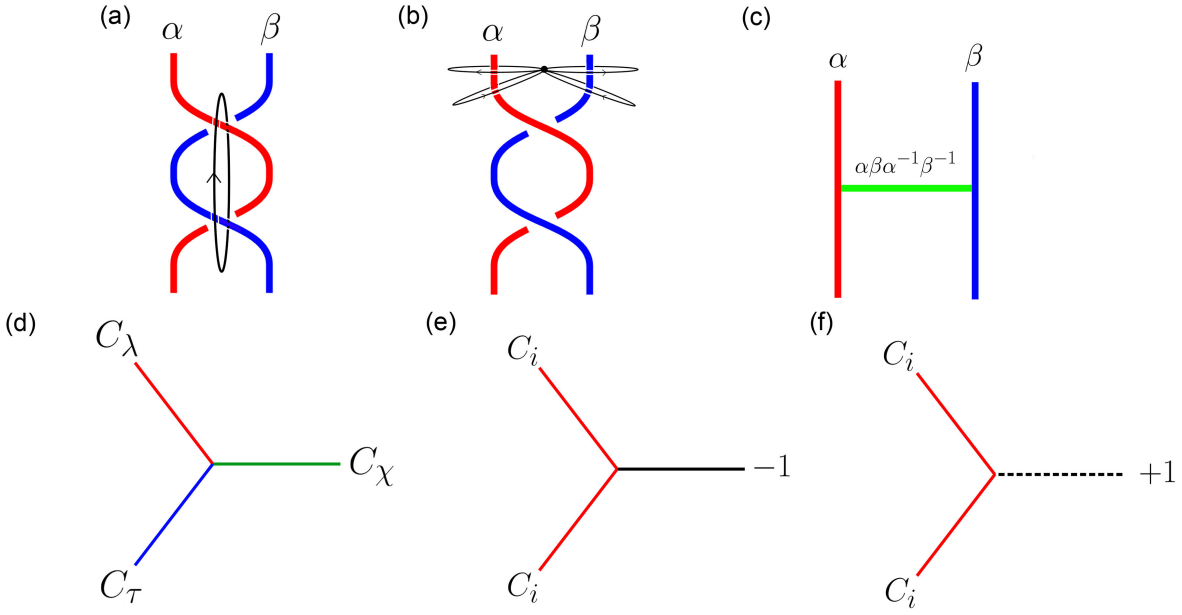

FIG. 4. (a) Braided structure formed by two defect lines of conjugacy classes α and β. The black loop classifies the homotopy class of the braided crossing. (b) The black loop can be isotopically deformed to the equivalent set of four loops shown (see Video 1) which reveals that pulling the lines apart results in a third defect of charge given by the commutator of the two initial defects $[\alpha,\beta]=\alpha\beta\alpha^{-1}\beta^{-1}$ as shown in (c). (d)–(f) Three classes of trivalent junctions formed from the quaternion algebra. (d) Junction consisting of three disclinations belonging to three distinct conjugacy classes. (e),(f) Junctions that represent the path-dependent result of combining two disclinations in the same conjugacy class $C_\lambda^2=+1\oplus-1$, respectively. Note that similar junctions to (e) and (f) also exist for the C_τ and C_χ classes.

show that the configuration is equivalent to the commutator of the two defect classes [1,20,21] (Video 1).

To see this, suppose we take two defects $\alpha,\beta\in Q_8$ and braid them around each other as shown in Fig. 4(a). In order to figure out the topological classification of the effective defect generated by the braid, we may draw a loop c around the middle braid [see Fig. 4(a) and Video 1]. We may continuously deform c in such a way that we can form the collection of loops shown in Fig. 4(b). We recall that a loop around defect lines defines the topological charge of the defect, so each of these loops signifies different factors of the corresponding defect charge. In other words, if we were to pull apart the braid, the effective defect charge formed in the middle could be read off from the loops in Fig. 4(b) and it corresponds to the commutator

$$[\alpha,\beta]=\alpha\beta\alpha^{-1}\beta^{-1}. \tag{4}$$

Because of the structure of the quaternion group, this commutator can result only in either ±1 (see Table II). Technically, the commutator subgroup of Q_8 is $\mathbb{Z}_2$. The trivial result occurs when α and β belong to the same conjugacy class or one of the ±1 classes. On the other hand, when the two lines belong to different conjugacy classes, we obtain the nontrivial result -1. This means there are nontrivial entangled structures that are topologically stable to external perturbations.

Considering the chiral-to-biaxial nematic mapping described above, we can now pursue an experimental verification of this key classical prediction [1].

C. Junctions

Another important consequence of having a quaternionic fundamental group is the existence of nontrivial trivalent junctions. The algebra of the quaternion conjugacy classes states that combining two defects of two different classes ($\neq\pm1$) results in a defect in the third. This is simply a restatement of the usual cyclic identities of the quaternions, all contained within $ijk=-1$. These trivalent junctions provide elementary building blocks from which one can construct more complex structures, such as trivalent networks and lattices.

Table II shows the types of junctions possible. Quaternion elements have the property that $i^2=j^2=k^2=-1$, which in terms of conjugacy classes reads $C_\lambda^2=C_\tau^2=C_\chi^2=+1\oplus-1$, where we drop the degeneracy of 2. This leads to junctions of the type shown in Fig. 4(c), where two defects of the same conjugacy class meet with a -1 line. There is also a trivial junction joining two defects of the same class to the identity element.

D. Network structures

Among the possible complex structures there are nontrivial links and networks (Fig. 5). The simplest possible

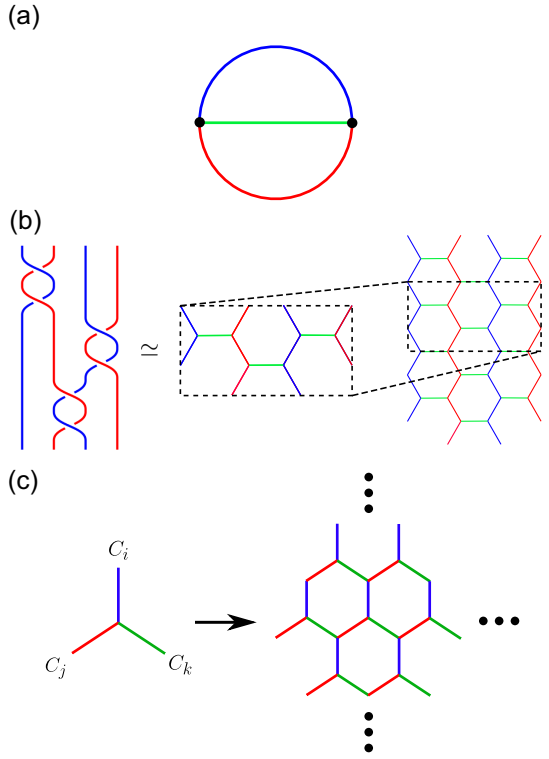

FIG. 5. (a) Simplest possible connected structure made from connecting all the free ends from the junction in (c) together. Note that such a structure can be obtained by "fusing" closed loops of two defect lines belonging to distinct classes. (b) Braided structure of four defect lines belonging to two different conjugacy classes gives rise to a topologically equivalent network "unit cell" where the green line belongs to the -1 class. This unit cell can be repeated to form a junction network (right). (c) A stable junction of three defect lines belonging to separate conjugacy classes also generates a unit cell for more complex lattice structures (right).

network can be realized minimally with two junctions. Take, for example, a (λ, τ, χ) junction in Fig. 4(d). One can take two legs and connect them on the third leg, creating a closed two-junction structure [see Fig. 5(a)].

Here we focus on more complex structures. One such structure can be realized from the entanglement viewpoint as follows: Considering several defect lines of alternating defect classes, we then perform the braid operation shown in the left-hand side of Fig. 5(b). This structure is topologically equivalent to the set of junctions shown in the right of Fig. 5(b). Such a structure can then be repeated to form an arbitrarily large hexagonal network, which can be seen as either a network or a braid. Similarly, one can create a repeating network of (λ, τ, χ) junctions as shown in Fig. 5(c). In practice, implementation of such networks will have the topology shown in Fig. 5, although the geometry may not be exactly hexagonal due to energetic differences in the elastic tension of each defect line following from the precise values of the elastic constants in the energy modeling below Eq. (8).

VI. METHODS

A. Simulations

1. Numerical simulations

We model the CLC equilibrium structures by numerical minimization of the Landau–de Gennes expansion of bulk free-energy density, including terms given by Eqs. (2) and (3) and the thermotropic term governing the isotropic-nematic phase behavior:

$$F_{\text{bulk}} = \int \mathrm{d}r^3 \left(\frac{A}{2}\mathrm{Tr}(\mathbf{Q}^2) + \frac{B}{3}\mathrm{Tr}(\mathbf{Q}^3) + \frac{C}{4}\mathrm{Tr}(\mathbf{Q}^2)^2 + f_{\text{elastic}} + f_{\text{chiral}} \right), \tag{5}$$

where $\mathbf{Q}$ is the tensorial order parameter; A, B, and C are parameters related to the isotropic-uniaxial phase behavior of CLCs [25,45,46]. Here we consider only the nematic-isotropic transition for a chiral nematic system and keep up to fourth-order terms. Without higher-order (fifth and sixth) terms and with biaxiality dominated by f_{chiral}, we have a precise mapping of chiral and biaxial director structures shown in Fig. 1.

Surface boundary conditions $\mathbf{Q}^0$ for $\mathbf{Q}$ are added to the calculation of the total energy via

$$F_{\text{surface}} = \int \mathrm{d}r^2 \frac{W}{2}(\mathbf{Q} - \mathbf{Q}^0)^2$$
$$Q^0_{ij} = S^0\left(n^0_i n^0_j - \frac{\delta_{ij}}{3}\right) \tag{6}$$

with W being a surface anchoring coefficient. $\mathbf{Q}^0$, the preferred order-parameter value on the surface, is calculated according to the surface pattern $\mathbf{n}^0$, which varies from uniformly planar alignment to one containing half-integer defects or twist walls depending on experimental designs (see Sec. VI B 2 below). S^0 is set using the expected equilibrium values in bulk. We found that controlling surface biaxiality T^0 and $\mathbf{m}^0$ was unnecessary in our system, where $\mathbf{m}$ spontaneously aligns with the helical axis in bulk during energy relaxation.

Equilibrium structures are found based on a gradient descent method with a finite-difference mesh [47], using a home-built MATLAB program provided in Ref. [11]. The director fields and the uniaxial and biaxial order parameters are obtained by identifying the eigenvalues λ_i and eigenvectors $\mathbf{v}_i$ of the tensor $\mathbf{Q}$ [see Eq. (1)] at each grid point:

$$S = \lambda_1 - \lambda_3,$$
$$\mathbf{n} = \mathbf{v}_1,$$
$$T = \lambda_2 - \lambda_3,$$
$$\mathbf{m} = \mathbf{v}_2, \tag{7}$$

with $\lambda_1 > \lambda_2 > \lambda_3$ and corresponding $\mathbf{v}_i$, $i = 1$–3 being the eigenpairs of the energy-minimizing $\mathbf{Q}$. The third director is then $\mathbf{l} = \mathbf{n} \times \mathbf{m}$. In the approach described here, our biaxiality analysis and interpretation of disclinations is not hindered by the emergence of vanishing biaxiality or reverse twisting at point defects [48], and the biaxial topology prescribed by chirality is consistent throughout the volume since it is energetically costly to fully unwind all the twist structure to a uniformly aligned state, even with such small biaxiality T.

In the examples illustrated in this work, the following parameter values were used [11,49,50]: $A = -1.72 \times 10^5$ J/m^3, $B = -2.12 \times 10^6$ J/m^3, $C = 1.73 \times 10^6$ J/m^3, $\gamma_1 = 7.4$ pN, $\gamma_2 = 12$ pN, $\gamma_4 = -0.0017$ N/m, $\gamma_6 = 11.9$ pN, and $W = 10^{-3}$ J/m^2. These constants give an equilibrium $S \approx 0.6$ and $T \approx 0.001$. Note that a negative γ_4 represents left-handed chirality in our numerical model.

2. Numerical visualization

The analysis and visualization of disclination positions were performed in MATLAB by rendering the smoothness of the director fields. For instance, a λ disclination is represented by discontinuity in the $\boldsymbol{\chi}$ and $\boldsymbol{\tau}$ director fields but not in the $\boldsymbol{\lambda}$ field [51]. τ disclinations, likewise, are revealed by finding regions with a continuous $\boldsymbol{\tau}$ field but singularities in the $\boldsymbol{\lambda}$ and $\boldsymbol{\chi}$ fields. In practice, we quantified the smoothness of a director field based on the inner product of the directors at neighboring grid points.

Another more conceptually straightforward, but more computationally intensive approach, is to calculate the actual topological winding numbers in the three director fields for all grid points. A λ disclination is then identified by vanishing winding number in $\boldsymbol{\lambda}$ but nonzero ($\pm\frac{1}{2}$) winding in the other two director fields. The contour regions of director smoothness, or winding number, are plotted for each field individually and then superimposed. The two methods give consistent results.

For defects in which the helical axis director $\boldsymbol{\chi}$ is not uniquely defined [52], we performed the visualization based instead on the matching biaxial directors $(\mathbf{n}, \mathbf{m}, \mathbf{l})$ (see Sec. II) obtained from tensor diagonalization [Eq. (7)]. In some cases, we manually picked the combination of regions and one of the two director sets to circumvent numerical artifacts.

B. Experimental techniques

1. Sample preparation

The CLC cells in our work were made of two glass slides or coverslips, both chemically treated to have a specifically designed surface anchoring determined by the boundary conditions for the LC molecular directors. Specifically, 1.0 wt % (weight percentage) of poly(vinyl alcohol) (PVA, Sigma-Aldrich) in water was used to generate a unidirectional parallel configuration for the CLC directors, and an azobenzene dye SD1 1.0 wt % in dimethylformamide was applied for photoalignment [53,54]. Chemical solutions were evenly spread on the glass surfaces by spin coating at 700 rpm for 15 s then 3000 rpm for 45 s, followed by heating at 100 °C for 1 min to thoroughly evaporate the solvents. For PVA-coated surfaces, the anchoring direction was defined by gently rubbing a piece of cloth against the surface along the desired anchoring direction. The boundary conditions for SD1-treated glasses, on the other hand, were designed using photoalignment techniques (detailed below) [53,54].

The gap distance between the two glass pieces was set by silica spacer spheres (with diameters ranging from 7 to 40 μm, from Thermo Fisher). The CLC sandwiched between them was prepared by doping cholesterol pelargonate (Sigma-Aldrich) into 4-Cyano-4'-pentylbiphenyl (5CB, EM Chemicals) to form a left-handed CLC and subsequently used to fill the glass cells. The cholesteric pitch p controlled by the doping concentration ranged from 2 to 10 μm. To control the positions of disclinations (which is pinned to the surface; see photopatterning below) after the CLC filling, the top glass was shifted or reoriented using a steel tweezer under the microscope.

2. Photopatterning of the confining surface

To precisely control the types and locations of defects, we photopatterned the SD1-coated surfaces with topologically nontrivial boundary conditions. Specifically, surface patterns with topological point defects or domain walls were imprinted to facilitate the formation of disclinations. Each half-integer defect imprinted on the surface served as a pinning point for one disclination, which provides control over the start and end positions of the disclination [53,55]. Twist domain walls, on the other hand, help induce layer dislocations such as bounded $\lambda\tau$ pairs (by π-twist wall) or -1 disclinations (by 2π-twist wall) in CLC within planar cells [31,56,57].

With the designed surface director alignment, the photoresponsive azobenzene dye was locally reoriented by polarized blue light to render it perpendicular to the incident polarization in the controlled illumination area. We performed the illumination with a commercial microdisplay and generated configurations based on identifying regions with the same director orientations in the predesigned director boundary conditions [58]. The optical alignment involved a wave plate and a polarizer to adjust the polarization of the illumination light and a 4× objective (numerical aperture, NA 0.13) to focus the light on our sample glass surface. The detailed optical setup for photopatterning can be found in Refs. [53,58]. CLCs were subsequently introduced into the glass cell, after which we found the reorientation of azobenzene dye to be negligible. In our experiments with a uniform background far field, the helical axis stayed perpendicular to the substrate throughout the photopatterned areas.

3. Microscopy

To observe non-Abelian defects, a charge-coupled-device camera (PointGrey) mounted on inverted microscopes (Olympus, IX-83) with 4× objective (Olympus, NA 0.13) was used for optical microscopy, such as bright-field imaging. Polarizers and a phase ring were inserted for polarizing optical microscopy and phase contrast microscopy, respectively. Three-photon excited fluorescence polarizing microscopy (3 PEF PM) [59] was also carried out to verify the molecular director $\boldsymbol{\lambda}$ configuration around defects. In brief, the three-photon excitation of the 5CB molecules involved the incident light generated from a Ti:sapphire pulse laser (Chameleon Ultra II, Coherent) operating at 870-nm wavelength passing through a linear polarizer, and the fluorescence signal was epicollected using a 60× objective (Olympus, NA 1.35) and magnified by a photomultiplier tube (H5784-20, Hamamatsu). In the three-photon process, the fluorescence intensity scaled as $\cos^6\theta_n$, where the angle θ_n was the angle made by the 5CB molecular director $\boldsymbol{\lambda}$ with the polarization of the excitation light. The microscopy was thus used to probe the director alignment, and numerical simulations of 3 PEF-PM images were performed accordingly.

VII. RESULTS

The quaternion algebra governing biaxial defects contains three classes of three-defect junctions [see Fig. 4(d)]. Here, we describe the observations and analysis of such structures in both computer simulations and experiments. While experimentally, various junctions are observed in unconstrained sample geometries, they are typically uncontrolled transient features of polydomain samples. In contrast, our surface photopatterning approach allows us to pin the end points of these defect lines so that their structure can be thoroughly analyzed.

A. (λ, τ, χ) junctions

We first simulate a chiral nematic system with the methods laid out in Sec. VI A. Figure 6 shows two different simulated (λ, τ, χ) junctions corresponding to the processes in Fig. 6(a) $\tau^-\lambda^+ \leftrightarrow \chi^-$ and Fig. 6(b) $\tau^- \leftrightarrow \chi^-\lambda^-$. These disclination junctions are not only topologically stable but also energetically robust against thermal fluctuations with the chosen numerical parameters. Figure 6(c) and Videos 2 and 3 show the complete set of junction types that are numerically observed and energetically relaxed for a left-handed CLC. Though one would expect that defects are free to deform to all the topologically equivalent structures conserved in such a soft fluid system, we note that the energy-minimizing junction structures obtained from computation inherit chirality from the underlying molecular chiral nematic host medium. The mirror images of these junctions were found numerically to exist in right-handed CLCs, thus providing an extra control knob for chiral biaxial systems. In addition, the structure of a bound pair

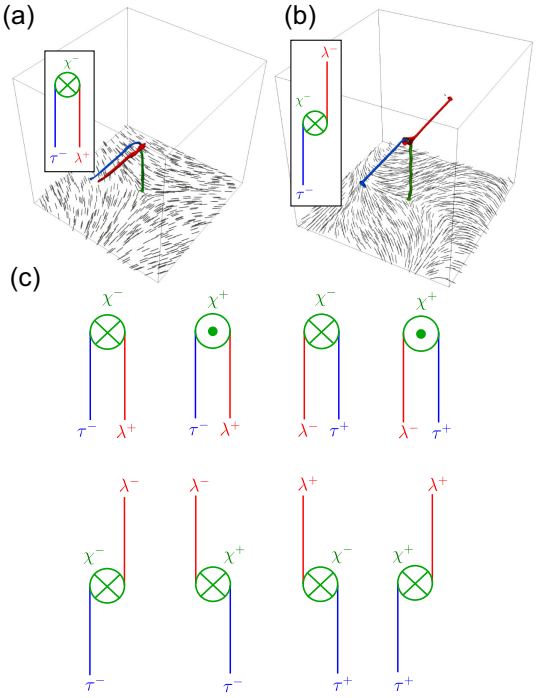

FIG. 6. (a),(b) Numerically simulated $\chi/\lambda/\tau$ threefold junctions for the cases (a) $\tau^-\lambda^+ \leftrightarrow \chi^-$ and (b) $\tau^- \leftrightarrow \chi^-\lambda^-$ with their respective diagrams shown. The results are obtained from the minimization of the Landau–de Gennes energy (see Sec. VI) with the $\boldsymbol{\lambda}$ director field on the bottom surface rendered in black rod patterns corresponding to the experimental photopatterning of the same field structure. (c) Schematic representations of eight geometries of junctions obtained from the numerical computation of a left-handed chiral nematic LC. Here, the direction of the χ disclination is represented by a cross and a dot for into and out of the page, respectively.

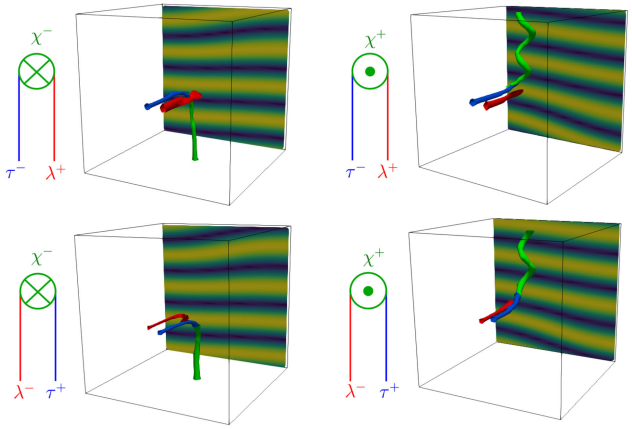

VIDEO 2. Visualization of the director field near the simulated $\chi/\lambda/\tau$ threefold junctions in a left-handed CLC. Each schematic shows the defect types and orientations. The moving vertical cross section is colored according to nematic director orientation (yellow for $\boldsymbol{\lambda}$ parallel to the moving direction; dark blue for $\boldsymbol{\lambda}$ perpendicular to all three disclinations).

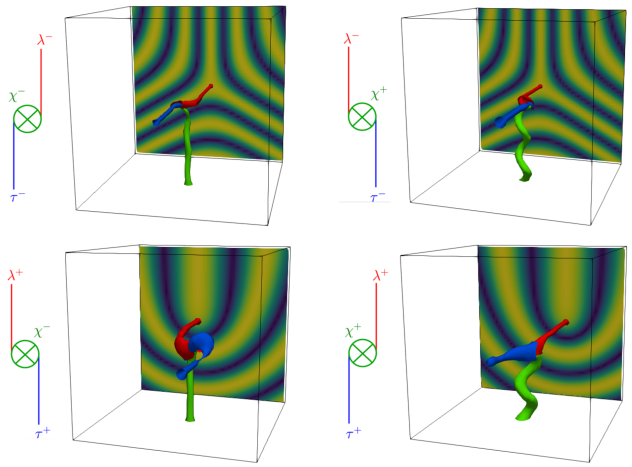

VIDEO 3. Visualization of helical layers near T-shaped threefold junctions in a left-handed CLC.

of parallel λ and τ disclinations (side by side) can be found in Fig. 6(c) top row with notable energetic stability. In Sec. VIII B, we argue that the chirality of the system provides the elastic tension required for the formation of stable bound states of defects.

The threefold junctions discussed so far consist of one λ, one χ, and one τ disclination, that is, all of the classes shown in Fig. 4(d). Beyond the single-junction (elementary) structures, multijunction structures were also numerically stabilized by gluing junctions with matching topology and geometry. Figures 7(a) and 7(b), for example, show how a χ disclination splits into a parallel pair of λ and τ defects, which then merge to form a χ again. Interestingly, numerical minimization of the free energy suggests that there is a preference for χ^- or χ^+ depending on the relative orientation of the defects. In other words, energy-minimizing structures of multiple junctions are assembled from connections of the geometries found in Fig. 6(c). As a result, we found that χ defects connected at the same side of the numerical volume tended to have the opposite signs [Fig. 7(a)], and conversely, χ lines with the same sign extended out in different directions as in Fig. 7(b). This feature of the junction geometry is further confirmed experimentally later below.

Threefold junctions can also serve as the building blocks for multijunction disclination networks, such as those shown in Fig. 5. By properly joining individual defect junctions, we numerically realized multijunction networks that could be repeated to build infinitely large networks [Figs. 7(c) and 7(d)]. Note that the equilibrium structure of χ^+ in numerical simulations is a spiral-like trace of the disclination core due to the strong elastic anisotropy [$K_1, K_3 > K_2$ in Eq. (8) below], while χ^- is straight and has lower elastic energy cost, as shown in Fig. 7.

Experimentally, we also generated defect junctions and robustly controlled disclination orientations by surface patterning techniques (see Sec. VI). Figure 8 shows a trijunction depicting the process $\chi^- \leftrightarrow \lambda^+\tau^-$, with the χ

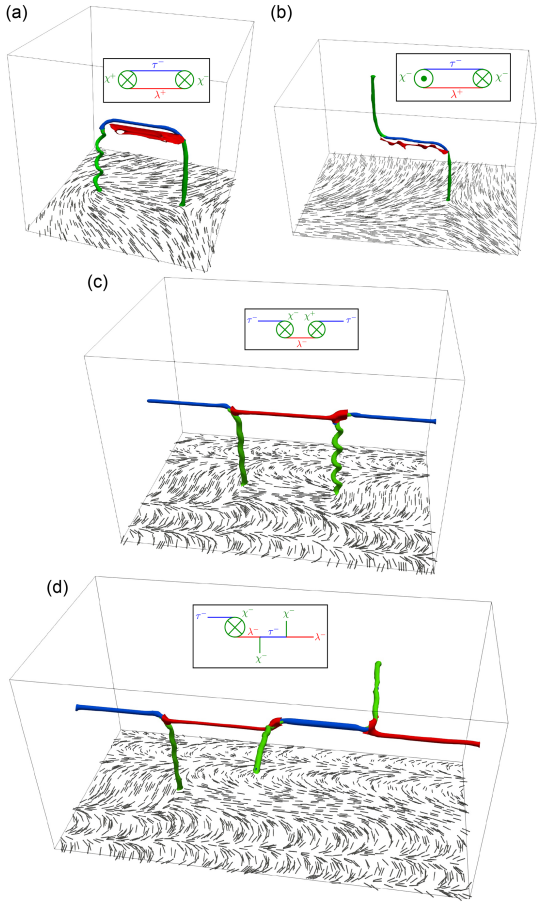

FIG. 7. Examples of numerically modeled disclination structures based on (χ, λ, τ) junctions with their corresponding diagrammatic representations and $\boldsymbol{\lambda}$ fields on the bottom surfaces shown. (a),(b) Two examples of joined elementary trijunctions with χ disclination ending on the surfaces. (c),(d) Two examples of a composite junction series comprised of two and three elementary junctions, respectively, can be extended to larger disclination networks.

disclination attached to the bottom surface. Since the χ is parallel to the viewing direction under the microscope [along z, Fig. 8(b)], it renders a dark spot where the $\lambda^+\tau^-$ defects terminate, characterized by the color contrast in POM. Note that among the simulated junctions [Fig. 6(c)], this form ($\chi^- \leftrightarrow \lambda^+\tau^-$) is most energetically favored due to the strong anisotropy of the system [31] and thus is frequently observed in numerics and experiments.

Furthermore, consistent numerical simulations of 3 PEF-PM (see Sec. VI) images were performed, which effectively revealed and confirmed the director configurations [59]. We compared the director configuration around a defect junction in the whole 3D volume shown in Fig. 8(a), which appears like a color contrast reaching an end under POM [Fig. 8(b)]. Good agreement is found between the computational and empirical results of the fluorescence signal, including the representative 2D slices in Figs. 8(c) and 8(d) parallel or perpendicular to the $\lambda\tau$ pair. Figure 8(e) shows the director configuration around a disclination pair, with

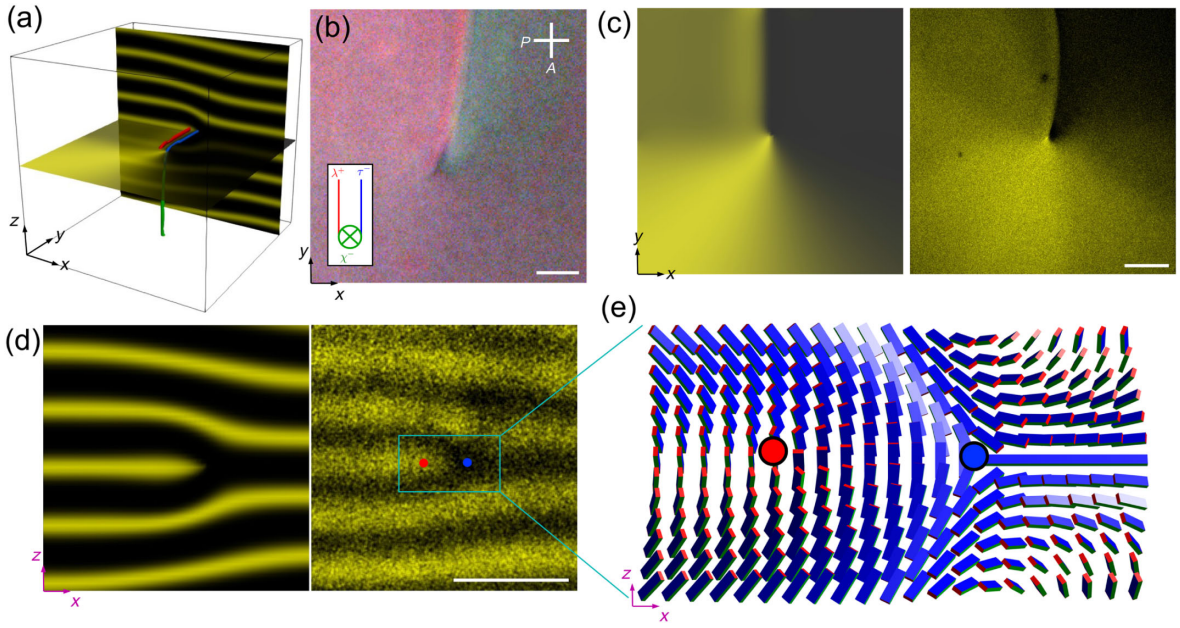

FIG. 8. (a) A defect junction visualized in computer simulations. (b) Experimental top view of such a defect junction obtained with POM. Diagrammatic representation of the junction; orientations of polarizer and analyzer are marked. (c),(d) Simulated (left) and experimental (right) three-photon excitation fluorescence polarizing microscopy (3 PEF-PM) images along or across the $\lambda - \tau$ disclination pair. The slice planes correspond to those in (a). (e) An enlarged brick visualization where brick edges represent biaxial director fields (from long to short: **n**, **m**, **l**, respectively). The 3 PEF-PM signal is strongest when molecular director **n** is aligned along the y direction (see Sec. VI). The junction structure is also described as a dislocation in systems viewed as chiral nematic quasilayers. All scale bars are 5 μm.

bricks showing red faces indicating **n** along the y direction and a stronger 3 PEF-PM signal in Fig. 8(d). This structure for **n** is often found with mismatching helical layers and resembles a dislocation, as evident in Fig. 8(d). This provides an *in situ* verification of the simulated defect structures as well as immediate identification of junction types. Since the vertical χ^- connects to the bottom surface with the $-1/2$ winding number, we will label the surface pinning site as $-$ for the experiments with multiple junctions demonstrated below.

As shown in Figs. 7(a) and 7(b), the preferred geometries of the defect connections in equilibrium are a combination of the junctions in Fig. 6(c) with matching types and orientations of defects. Accordingly, by focusing on cleanly separated elementary defects (χ), we see a selective connection to the surface pinning defects in Fig. 9. Simply put, "defects with the same topological charge connect on opposite surfaces, while defects with opposite charges connect on the same surface," as summarized schematically in Fig. 9(a). The case of opposite charge adds a handle to the boundary surface, providing a means of communicating between spatially separated points on the boundary via the bulk. The case of same charge defects allows one boundary surface to connect to a distant boundary via a line defect passing between them. We then designed an experiment based on such selective defect connections [Figs. 9(b)–9(g)]. The preprinted pinning surface defects with $+1/2$ or $-1/2$ winding number are placed in several relative positions. Figures 9(b) and 9(c), for instance, show that defects (each being $\lambda\tau \equiv \chi$) extend across the sample area to have larger disclination length instead of connecting to nearby surface defects. In contrast to a typical soft matter system where energy-costly defects would be shortened whenever possible, here the selective connections of disclinations are a result of the interplay between the non-Abelian biaxial topology and the geometry of non-Abelian defect junctions, on top of energetic considerations in a CLC. Furthermore, by simply rotating the upper glass substrate [Figs. 9(d)–9(g)], we clearly observed disclination arrangements being "same charge xor (i.e., exclusive or) same surface" as summarized in Fig. 9(a), consistent with our interpretation of non-Abelian defect topology in CLCs. Thicker and brighter under the microscope [31,60], ± 1 lines enable more complex arrangement of disclinations. For instance, we additionally found junctions connecting four $+1/2$ surface defects such as those in Figs. 9(h) and 9(i). With two $+1/2$ surface defects on each side of the substrate, the central segment linked to multiple χ lines is interpreted depending on its connection: The segment is -1 if defects from the same surface merge first as in Fig. 9(h), or $+1$ is assigned instead if χ connects across surfaces and the middle segment is topologically trivial and free to remove [Fig. 9(i)], consistent with the theory prediction in Figs. 4(e) and 4(f). Below, we perform more detailed analyses on defect junctions containing -1.

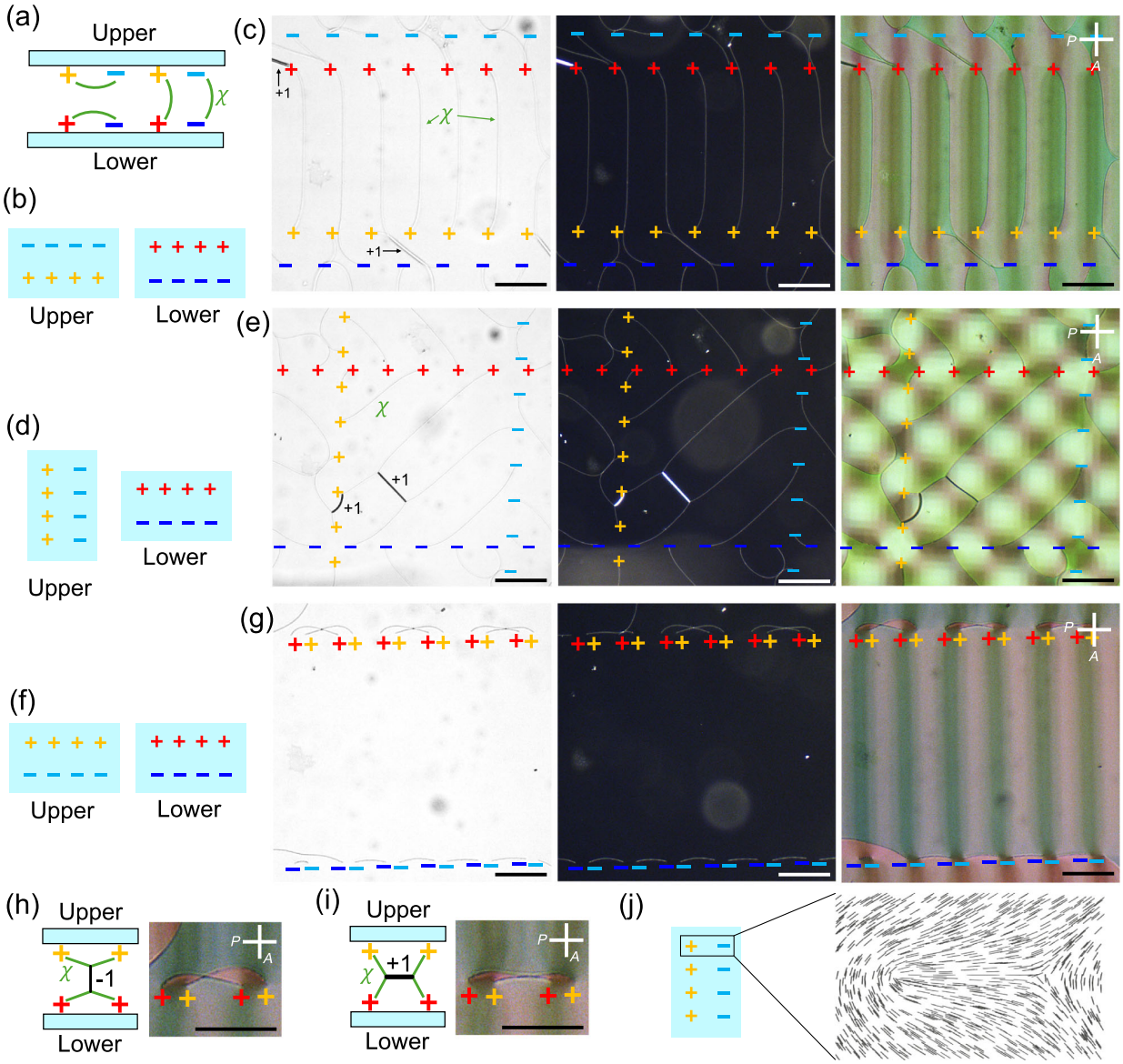

FIG. 9. (a) Topologically selected defect connections (through χ, green curves) based on the junction geometries in Fig. 6(c). The isolated, uninterfered defect lines connect only two defects on the same surface or with the same sign, but not both. The "+" and "−" signs represent surface point defects with winding number $\pm 1/2$, respectively. Defects on different surfaces are distinguished by colors. (b),(d),(f) Schematics representing the upper and lower boundary conditions for LC directors with half-integer defects, which serve as pinning sites for the disclinations. (c),(e),(g) Corresponding connections through disclinations between surface defects when upper and lower glass plates are overlaid. From left to right, images of the same area are taken using bright-field, phase contrast, and polarizing optical microscopy. (h),(i) The defect junctions that involve four surface defects and elements ± 1. (j) Pattern used for photoalignment of the molecular λ director field on confining glass surfaces. Cholesteric pitch $p = 7.4$ μm, cell thickness $d = 50$ μm, and scale bars are 300 μm.

B. $(\chi, \chi, -1)$ junction

Another important type of trijunction beyond the class with one each of λ, χ, and τ disclinations discussed above is that resulting from the entanglement of two defects—algebraically equivalent to the negation of a group element [Fig. 4(e)]. Experimental realizations of this junction are shown in Fig. 10. For the crossover of a χ^+ disclination with a -1 disclination, see Figs. 10(a)–10(c). The individual creations of a χ line and a -1 defect on separated glass surfaces guaranteed the correct assignments of quaternion group elements (see Sec. VI). The crossing was then created by overlapping the two glass surfaces with their relative position carefully adjusted under the microscope. Near the defect crossing, the overall elastic energy is reduced by rendering the two defects parallel. Brightness and color contrast, however, allow for an unambiguous

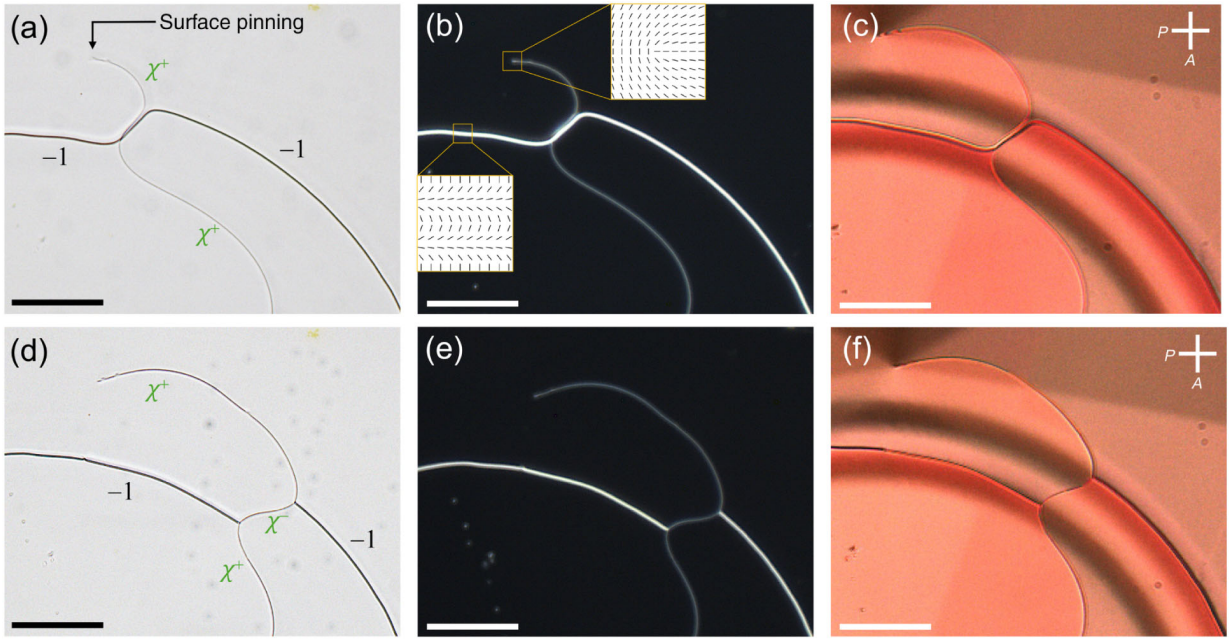

FIG. 10. (a)–(c) Crossover of a -1 and χ^+ disclination imaged using (a) bright field, (b) phase contrast, and (c) POM, respectively. The χ^+ line ends at a surface pinning point defect on the upper boundary of the CLC sample (see Sec. VI). (d)–(f) Two topologically stable threefold junctions formed from merging the crossover in (a)–(c) accompanied by the generation of χ^- (see Video 4). Insets in (b) show the surface alignment of the molecular director $\boldsymbol{\lambda}$ field. Orientations of the polarizers are marked in (c),(f), cholesteric pitch $p = 7.4$ μm, cell thickness $d = 50$ μm, and scale bars are 100 μm. The displacement of the junctions is due to the fluidity in our soft matter system.

identification of the two distinct defect classes (Fig. 10). By locally melting the CLC with laser tweezers near the defect crossing (Video 4), and then allowing the system to reorient in a quench, we produced a set of two connected threefold junctions [Figs. 10(d)–10(f)] of the $(\chi,\chi,-1)$ class. As evidenced by the microscopic characterization Figs. 10(d)–10(f), the two junctions are connected by a χ line corresponding to the defect algebra $\chi^+ \times -1 = \chi^-$ following Table I. We also assessed the topological stability of these junctions by repeated laser-tweezer-based heating and mechanical excitations: We found these $(\chi,\chi,-1)$ junctions to be unbreakable due to the topological protection imposed by intrinsic biaxiality. Furthermore, by recognizing this -1 defect as a combination of two parallel λ disclinations, given its resemblance to a dislocation of one helical layer [31], we can associate the $(\chi,\chi,-1)$ defect junction with a $\chi\chi \leftrightarrow \lambda\lambda$ process. We want to note that, however, such examples of -1 defect structure are different from those discussed in Ref. [30], in which case, the process of $\chi\chi \leftrightarrow \lambda\lambda$ is shown to be nontrivial.

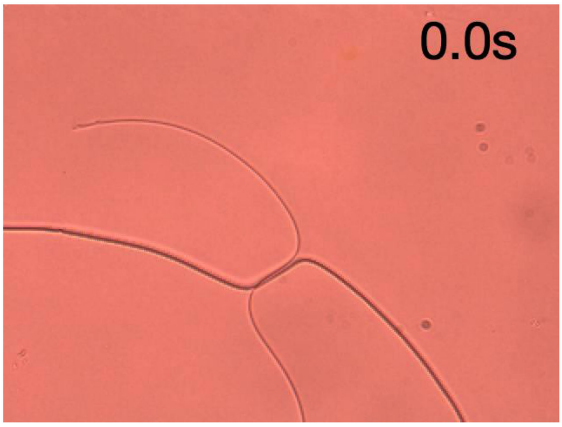

VIDEO 4. Laser tweezer manipulation of a defect line crossing formed by -1 (thick) and χ^+ (thin) disclinations under microscopy, showing a real-time $\chi^+ \times -1 \longrightarrow \chi^-$ process.

Following the discussion in Sec. V C, we also exploited the robustness of the single-junction structure to experimentally construct a topologically stable network with $(\chi,\chi,-1)$ defect junctions as building blocks [Figs. 11(a)–11(c)]. To create the defect network, we defined the surface boundary conditions that contains an array of π-twist walls [Fig. 11(d)]. By controlling the width and separation distances of the twist walls, manipulation of the surface pattern controls the formation of defect junctions. Specifically, larger distances between and sizes of π-twist walls prefer forming χ defects, while smaller distances and sizes (essentially become a 2π-twist wall) generate a -1 line instead (see Sec. VI). As presented in Fig. 11, the χ and -1 defects are characterized and easily distinguished microscopically. The experimental realization of the network is expandable by including more repeating units of the surface pattern, reconfigurable by employing laser tweezers, and most importantly, always topologically stable as guaranteed by the non-Abelian biaxial topology of the fundamental group elements of CLCs.

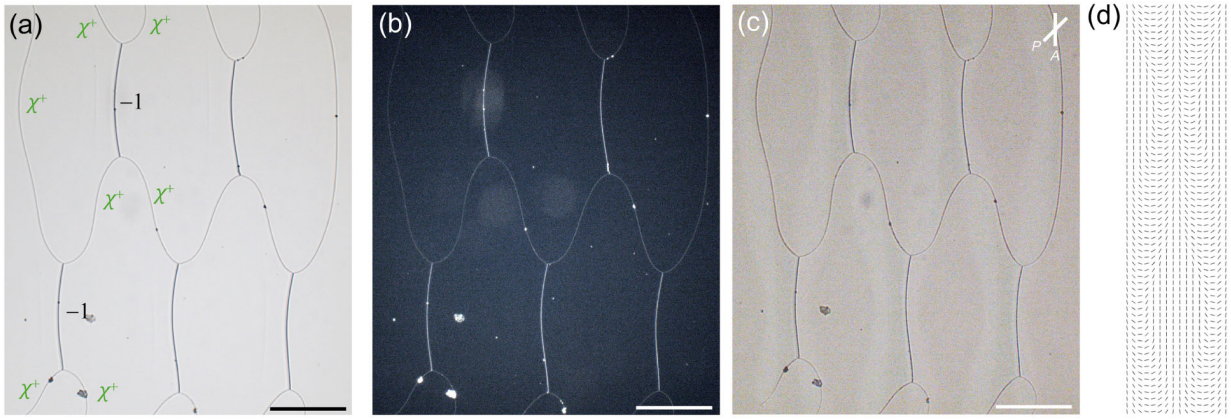

FIG. 11. (a)–(c) Experimental realization of a stable disclination network based on the $(\chi,\chi,-1)$ junctions imaged using (a) bright-field, (b) phase contrast, and (c) polarized optical microscopy, respectively. (d) A repeating unit of the designed surface alignment with changing distance between two π-twist walls. Cholesteric pitch $p = 7.4$ μm, cell thickness $d = 50$ μm, and scale bars are 300 μm.

VIII. RIGIDITY OF CHIRALITY-INDUCED BIAXIALITY IN D2CLCS

The biaxiality in our system is dominated by the twisting alignment of molecules. It is thus important to investigate the robustness of such biaxiality; for example, here we assume a weak but persistent biaxial order contributed solely from the chiral nature in CLCs. Below, we analytically demonstrate how the chirality contributes to biaxial elastic moduli, and based on such a relation, the role of chirality in stabilizing a bound state of biaxial disclinations that is widely observed in both lab and simulation.

A. Biaxial elasticities of chiral nematics

The mapping of the chiral and biaxial director fields, as introduced in Sec. II, allows us to use the biaxial free energy written in terms of derivatives of the orthonormal directors $(\mathbf{n},\mathbf{m},\mathbf{l})$ to describe a CLC [26],

$$\begin{aligned} f^{\mathrm{FO}}_{\mathrm{elastic}} = {} & \frac{K_1}{2}(\nabla\cdot\mathbf{n})^2 + \frac{K_2}{2}(\mathbf{n}\cdot\nabla\times\mathbf{n})^2 + \frac{K_3}{2}(\mathbf{n}\times\nabla\times\mathbf{n})^2 + \frac{K_4}{2}(\nabla\cdot\mathbf{m})^2 + \frac{K_5}{2}(\mathbf{m}\cdot\nabla\times\mathbf{m})^2 + \frac{K_6}{2}(\mathbf{m}\times\nabla\times\mathbf{m})^2 \\ & + \frac{K_7}{2}[\mathbf{n}\cdot(\mathbf{m}\times\nabla\times\mathbf{m})]^2 + \frac{K_8}{2}[\mathbf{m}\cdot(\mathbf{n}\times\nabla\times\mathbf{n})]^2 + \frac{K_9}{2}[\mathbf{m}\cdot\nabla\times\mathbf{l}]^2 + \frac{K_{(10)}}{2}[\mathbf{n}\cdot\nabla\times\mathbf{l}]^2 \\ & + \frac{K_{(11)}}{2}(\nabla\times\mathbf{l})^2 + \frac{K_{(12)}}{2}(\nabla\cdot\mathbf{l})^2, \end{aligned} \tag{8}$$

with the first three terms resembling the uniaxial Frank-Oseen model: K_1, K_2, K_3 are the elastic constants for splay, twist, and bend deformations, respectively.

By expanding the tensor-based Eq. (2) and comparing to the director-based Eq. (8), one can relate the two elastic models and write the elastic constants K_i (in the biaxial director model) in terms of γ_i in the tensorial model (see Appendix B). This yields a biaxial description of the elastic properties of chiral nematics. Since the intrinsic biaxiality of our chiral liquid crystal is much smaller than its uniaxiality order parameter $T \ll S$, we can further approximate the coefficients $\gamma_i, i = 1, 2, 6$ as [61]

$$\begin{aligned} \gamma_1 &= \frac{1}{12S^2}(3K_2 + K_3 - K_1), \\ \gamma_2 &= \frac{1}{2S^2}(K_1 - K_2), \\ \gamma_6 &= \frac{1}{4S^3}(K_3 - K_1), \end{aligned} \tag{9}$$

which give an estimation of the orthorhombic biaxial elastic moduli $K_i, i = 4$–12 up to $\mathcal{O}(T/S)$ for a CLC:

$$\begin{aligned}
K_4 &= \left(-\frac{1}{3}K_1 - \frac{2}{3}K_3\right)\frac{T}{S},\\
K_5 &= \left(\frac{2}{3}K_1 - K_2 - \frac{2}{3}K_3\right)\frac{T}{S},\\
K_6 &= \left(-\frac{1}{3}K_1 - \frac{2}{3}K_3\right)\frac{T}{S},\\
K_7 &= (K_3 - K_1)\frac{T}{S},\\
K_8 &= (K_1 - K_3)\frac{T}{S},\\
K_9 &= (2K_1 - K_2 - K_3)\frac{T}{S},\\
K_{(10)} &= (K_1 - K_2)\frac{T}{S},\\
K_{(11)} &= \left(K_2 + \frac{2}{3}K_3 - \frac{2}{3}K_1\right)\frac{T}{S},\\
K_{(12)} &= \left(\frac{1}{3}K_1 + \frac{2}{3}K_3\right)\frac{T}{S}.
\end{aligned} \tag{10}$$

Equation (10) represents the elastic moduli of orthorhombic biaxial nematics that originate purely from chirality, in addition to the intrinsic chiral deformations that might exist within such models (see Appendix B). We found that the elastic constants $K_i, i = 4$–12 scale proportionally to the biaxiality order parameter $\mathcal{O}(T)$, which is scaled as $T \propto q^2$ in single-component materials with chirality q [16]. Vanishing biaxiality reduces to the conventional uniaxial Frank-Oseen model (with only the first three elastic terms) as expected. On the other hand, the chirality-induced biaxiality [16,62–64] gives rise to elastic contributions beyond bend, twist, or splay in the molecular director field. Equation (10) is especially useful for studies where the precise measurement of biaxial elastic constants in the lab is challenging. Furthermore, this mapping of the elasticities of CLCs to biaxial nematics strengthens the fundamental connection of the two systems, allowing us to analytically model experimental observations of bound states as detailed below while using parameters measured in experiments.

B. Energetic stability of a bound state of two defect lines

We now analyze the bound state of two parallel defect lines within the elastic model given by Eq. (2). Bound states of this kind are seen experimentally and numerically in junctions such as in Figs. 6(a) and 8.

Suppose we have two defect lines with topological charge q_1 and q_2 separated by distance ρ in a cylindrical region $\Omega = D_R \times [0, L]$, where D_R is a disk of radius R. The region of interest away from the defect core with radius r_c is the annular region $r_c \ll r \ll R$. Here, the Q tensor may be continuously deformed to satisfy the sliding boundary condition $\partial_r Q_{ij} = 0$, which allows us to assume that the order parameter chiefly depends on the azimuthal angle. The elastic free-energy density can then be approximated by

$$f_{\text{elastic}} \approx \frac{f(\phi)}{r^2} + \frac{g(\phi)}{r}, \tag{11}$$

where $f(\phi)$ is the angular dependence of the expansion of the γ_1,γ_2, and γ_6 terms in Eq. (2). Similarly, $g(\phi)$ is the angular dependence of the chiral γ_4 term in Eq. (3). The free energy can now be approximated by integrating over the volume of Ω which, for convenience, can be split into three terms:

$$\mathcal{F} = \mathcal{F}_{q_1} + \mathcal{F}_{q_2} + \mathcal{F}_{q_3}. \tag{12}$$

The first two terms are identical up to the interchange $q_1 \leftrightarrow q_2$ and represent the individual energies of each defect. The radial integrals for these two terms are calculated in the annulus $r_c < r < \rho$ surrounding each defect line, as shown in Figs. 12(a) and 12(b), and take the form

$$\mathcal{F}_{q_{1,2}} \approx \int_0^L dz \int_0^{2\pi} d\phi \int_{r_c}^{\rho} r dr \left(\frac{f(\phi)}{r^2} + \frac{g(\phi)}{r}\right) \tag{13}$$

$$= \gamma_1 L S^2 K^{(1)}_{q_{1,2}} \ln\left(\frac{\rho}{r_c}\right) + \gamma_4 L S^2 (\rho - r_c) K^{(6)}_{q_{1,2}}. \tag{14}$$

Similarly, the third term is computed over the annular region $\rho < r < R$ surrounding the bound state [Fig. 12(c)]

$$\mathcal{F}_{q_3} \approx \int_0^L dz \int_0^{2\pi} d\phi \int_{\rho}^{R} r dr \left(\frac{f(\phi)}{r^2} + \frac{g(\phi)}{r}\right) \tag{15}$$

$$= \gamma_1 L S^2 K^{(1)}_{q_3} \ln\left(\frac{R}{\rho}\right) + \gamma_4 L S^2 (R - \rho) K^{(4)}_{q_3}, \tag{16}$$

where we have introduced the elastic constants associated with each defect class. They are obtained from the azimuthal integrals

$$\bar{K}^{(1)}_{q_i} \equiv F^{(1)}_{q_i}\left(\frac{T}{S}, \frac{\gamma_2}{\gamma_1}\right) + \frac{\gamma_6}{\gamma_1} S F^{(6)}_{q_i}\left(\frac{T}{S}\right) \tag{17}$$

$$\equiv K^{(1)}_{q_i} + \frac{\gamma_6}{\gamma_1} S K^{(6)}_{q_i}, \tag{18}$$

$$K^{(4)}_{q_i} \equiv G_{q_i}\left(\frac{T}{S}\right), \tag{19}$$

where the functions $F^{(1)}_{q_i}$ and $F^{(6)}_{q_i}$ are the azimuthal contributions of the γ_1, γ_2 terms and γ_6 term, respectively.

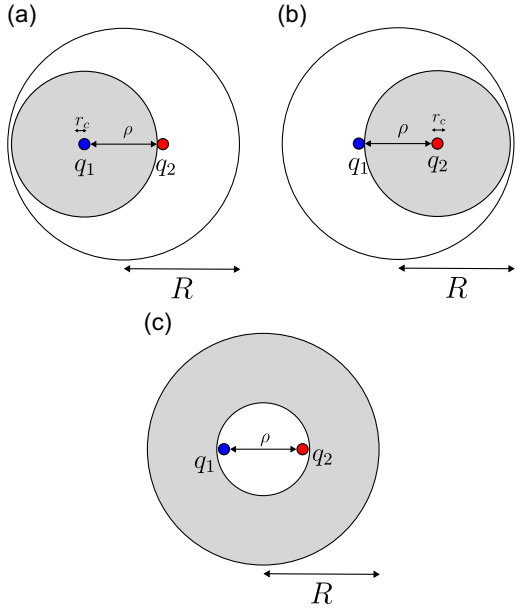

FIG. 12. Integration regions within the disc of radius R use to compute the integrals that define the free energies (a) $\mathcal{F}_{q1}$, (b) $\mathcal{F}_{q2}$, and $\mathcal{F}_{q3}$ in Eq. (12). The darker annular region shows the region in which the integrals are computed.

Similarly, G_{q_i} is the azimuthal contribution of the γ_4 term. Additionally, upon defining the elastic energy losses

$$\Delta\bar{K}^{(1)} \equiv \bar{K}^{(1)}_{q_1} + \bar{K}^{(1)}_{q_2} - \bar{K}^{(1)}_{q_3}, \tag{20}$$

$$\Delta K^{(4)} \equiv K^{(4)}_{q_1} + K^{(4)}_{q_2} - K^{(4)}_{q_3}. \tag{21}$$

The energy then becomes

$$\mathcal{F} = \gamma_1 S^2 L\left[\Delta\bar{K}^{(1)} \ln\left(\frac{\rho}{r_c}\right) + K^{(1)}_{q_3} \ln\left(\frac{R}{r_c}\right)\right] + \gamma_4 S^2 L[\Delta K^{(4)}(\rho - r_c) + K^{(4)}_{q_3}(R - r_c)]. \tag{22}$$

The minimum energy occurs at the separation

$$\rho_{\min} = -\frac{\gamma_1 \Delta\bar{K}^{(1)}}{\gamma_4 \Delta K^{(4)}}, \tag{23}$$

and the second derivative at this point is

$$\left.\frac{\partial^2 \mathcal{F}}{\partial \rho^2}\right|_{\rho_{\min}} = -\frac{\gamma_4^2 (\Delta K^{(4)})^2}{\gamma_1 \Delta\bar{K}^{(1)}}, \tag{24}$$

which requires $\Delta\bar{K}^{(1)} < 0$ corresponding to defect repulsion for $\rho_{\min}$ to be a minimum.

Recall that the sign of $\gamma_4 \propto q$ determines the handedness of the system. For $\gamma_4 > 0$, $\rho_{\min} > 0$ requires $\Delta K^{(4)} > 0$. On the other hand, if $\gamma_4 < 0$, we must have $\Delta K^{(4)} < 0$.

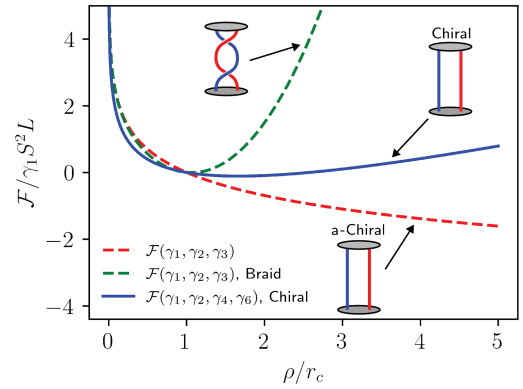

FIG. 13. Elastic free energy for three different bound-state configurations: (1) achiral, unbraided (red, dashed); (2) chiral, unbraided (blue, solid); (3) achiral, braided (green, dashed). Of the three, only the achiral, unbraided case does not have a stable minimum radius.

Seemingly, the sign of the $\Delta K^{(4)}$ term depends on the handedness. If we instead focus on the sign of the product $\gamma_4 \Delta K^{(4)}$, we see that it must be positive in both cases. This must be the case, because unlike the constants $\bar{K}^{(1)}_{q_i}$, which have some memory of the elastic moduli γ_1 and γ_6, the $K^{(4)}_{q_i}$ do not, as seen in Eq. (19). Thus, it is more appropriate to consider the sign of $\gamma_4 \Delta K^{(4)} > 0$ for a minimum to exist in the repulsive case, with $\Delta\bar{K}^{(1)} < 0$.

One can check that upon writing the elastic constants $K^{(1)}_{q_i}$ in terms of the Frank elastic constants in Eq. (8) and using the mapping described in Appendix B to relate to the biaxial coupling constants γ_i, the repulsive condition is satisfied subject to labeling the defects corresponding to C_λ with the smallest $K^{(1)}_{q_i}$. Doing the same for $K^{(4)}_{q_i}$ reveals that this condition is met when $T/S < 2/(\sqrt{5}-1)$.

Unlike the achiral nonanisotropic case in Ref. [65], where the repulsive condition leads to the energy being minimized when the defects are as far apart as possible, here we have an energy-minimizing separation distance that is stabilized within the bounds of the medium by none other than the elastic tension provided by the intrinsic chiral nature of the bulk. Figure 13 shows the energy in Eq. (22) along with the achiral braided and unbraided cases. This agrees with the observation of bound states of the λ and τ defect pairs in the D2CLCs.

We can further compare this observation to the braided achiral nonanisotropic case in which there is a stable minimum radius. The tension that creates the bound state in that case is provided by an extrinsic chirality generated by physically braiding the two defects.

IX. CONCLUSIONS

The non-Abelian properties of the three-dimensional line defects have been of interest for decades but rarely seen in

experiments [36,66–68]. Here we uncover new metastructural features of such systems and realize them in the laboratory in a chiral liquid crystal with orthorhombic biaxial symmetry breaking.

In particular, we show that the four nontrivial classes of line defects have several distinct realizations: They may be stand-alone elementary defects, bound states of two elementary defects, as well as elements of junctions, both single and extended networks, all consistent with the well-known quaternionic algebra that governs their classification and possible defect couplings.

In this way, we reveal features of such systems beyond those obvious from their well-known mathematical classification and point the way to the construction of even more elaborate topologically rigid structures that pose theoretical and experimental challenges and may well have technological utility. The demonstrated experimental embodiments of defect networks not only comply with topological rules and constraints but also feature low-free-energy states, showing how our specific physical system selects lowest-energy configurations out of all allowed by topology rules. Enhanced manipulation over director alignments, such as tilting χ [69], would facilitate the realization of more complex topological structures in D2CLC. In addition to the rich topological behaviors of the D2CLCs realized in our specific material system, future research on materials with atypical elasticities, such as CB7CB (1″,7″-bis(4-cyanobiphenyl-4′-yl)heptane) [70], could reveal other energetic pathways of non-Abelian algebra. In addition to defect junctions and networks, our system may allow for realizing non-Abelian analogs of combinatorial vortex lattices [71] that have not yet been observed experimentally.

ACKNOWLEDGMENTS

The experimental and numerical simulations research at University of Colorado Boulder was supported by the U.S. Department of Energy, Office of Basic Energy Sciences, Division of Materials Sciences and Engineering, under Contract No. DE-SC0019293 with the University of Colorado at Boulder. I. I. S. acknowledges the support of the International Institute for Sustainability with Knotted Chiral Meta Matter (Grant No. WPI-SKCM2) at Hiroshima University in Japan during part of his sabbatical stay when this article was under preparation. I. I. S. and J.-S. W. acknowledge the hospitality of the Kavli Institute for Theoretical Physics in Santa Barbara with support from the National Science Foundation under Grant No. NSF PHY-2309135. R. A. V. acknowledges support in part from the National Science Foundation under Grant No. NSF PHY-2309135 as well as the National Science Foundation California LSAMP Bridge to the Doctorate Fellowship under Grant No. HRD-1701365. We thank Randy Kamien for a careful reading of the manuscript and valuable comments.

J.-S. W. and R. A. V. contributed equally to this work

APPENDIX A: FUNDAMENTAL GROUP OF SYSTEMS WITH BIAXIAL SYMMETRY

The fact that biaxial nematic systems have disclinations whose algebra is that of the quaternion group Q_8 is well known and quoted with confidence. However, for the sake of self-containment, here we prove the statement. In a more mathematical language, we want to prove that

$$\pi_1(\mathrm{SO}(3)/D_2) \simeq Q_8. \tag{A1}$$

To do so, we require the following theorem which proves useful in computing homotopy groups of coset spaces:

Theorem 1. Let G be a simply connected Lie group with subgroup $H \leq G$ and identity component $H_0 \trianglelefteq G$. Then,

$$\pi_1(G/H) \simeq H/H_0. \tag{A2}$$

Proof of this statement establishes an isomorphism between the fundamental group and the quotient space H/H_0 by relating the loops in G/H based at H to paths in G from a connected piece of H to the piece that contains the identity H_0.

Theorem 1 allows one to compute $\pi_1(\mathrm{SO}(3)/D_2)$ by lifting to a universal cover map. This is

$$\mathrm{SO}(3) \longrightarrow \mathrm{SU}(2), \tag{A3}$$

$$D_2 \longrightarrow Q_8. \tag{A4}$$

Here, the covering map sends π rotations about each symmetry axis of the rectangle into π rotations in SU(2) parametrized by the Pauli matrices. The set of such rotations forms the lift of D_2, that is

$$\{\pm 1, \pm i\sigma_x, \pm i\sigma_y, \pm i\sigma_z\}, \tag{A5}$$

which is simply the group of quaternions Q_8.

Now, applying Theorem 1, we have $\pi_1(\mathrm{SO}(3)/D_2) \simeq \pi_1(\mathrm{SU}(2)/Q_8) \simeq Q_8/(Q_8)_0 = Q_8$ since $(Q_8)_0 = \{1\}$.

APPENDIX B: RELATION BETWEEN THE ELASTIC MODULI OF THE BIAXIAL Q-TENSOR MODEL AND THOSE OF THE VECTORIAL MODEL

In addition to the sum of 12 linearly independent bulk elastic terms in the biaxial director model Eq. (8), the chirality contribution to orientational elasticity is expressed as

$$
\begin{aligned}
f_{\text{chiral}}^{\text{FO}} &= K_{(13)}(\mathbf{n}\cdot\nabla\times\mathbf{n}) + K_{(14)}(\mathbf{m}\cdot\nabla\times\mathbf{m}) \\
&+ K_{(15)}(\mathbf{n}\times\mathbf{m})\cdot(\mathbf{m}\cdot\nabla)\mathbf{n} \\
&+ K_{(16)}(\mathbf{m}\times\mathbf{n})\cdot(\mathbf{n}\cdot\nabla)\mathbf{m} \\
&+ K_{(17)}(\mathbf{n}\times\mathbf{m})\cdot(\mathbf{m}\times\nabla\times\mathbf{n}-\mathbf{n}\times\nabla\times\mathbf{m}).
\end{aligned} \tag{B1}
$$

Together with Eq. (8), the total elastic free energy describes a chiral biaxial system characterized by the three orthonormal directors $\{\mathbf{n},\mathbf{m},\mathbf{l}\}$.

Following the approach similar to Ref. [61], the elastic constants in the Q-tensor model and the vectorial model, which describes energy in terms of gradients of director fields, can be related by expanding Eqs. (2) and (8) and collecting terms with the same invariants, which serve as linear-independent bases for the projection. Ignoring the surface terms (those with the form $\nabla\cdot f$ [26]), the equations read

$$
\begin{aligned}
K_1 &= \frac{2}{3}S[(S-T)(6\gamma_1+3\gamma_2)-2(S^2-ST+T^2)\gamma_6], \\
K_2 &= \frac{4}{3}S[3(S-T)\gamma_1-(S^2-ST+T^2)\gamma_6], \\
K_3 &= \frac{2}{3}S[(S-T)(6\gamma_1+3\gamma_2)+(4S^2-4ST-2T^2)\gamma_6], \\
K_4 &= -\frac{2}{3}T[(S-T)(6\gamma_1+3\gamma_2)+2(S^2-ST+T^2)\gamma_6], \\
K_5 &= -\frac{4}{3}T[3(S-T)\gamma_1+(S^2-ST+T^2)\gamma_6], \\
K_6 &= -\frac{2}{3}T[(S-T)(6\gamma_1+3\gamma_2)+(2S^2+4ST-4T^2)\gamma_6], \\
K_7 &= 4ST(S-T)\gamma_6, \\
K_8 &= 4ST(T-S)\gamma_6, \\
K_9 &= 2ST(\gamma_2-2S\gamma_6), \\
K_{(10)} &= 2ST(\gamma_2-2T\gamma_6), \\
K_{(11)} &= \frac{4}{3}ST[3\gamma_1+(S+T)\gamma_6], \\
K_{(12)} &= \frac{2}{3}ST[6\gamma_1+3\gamma_2+2(S+T)\gamma_6],
\end{aligned} \tag{B2}
$$

with scalars S and T being uniaxial and biaxial order parameters, respectively. Similarly, the chiral twisting parts (B1) have

$$
\begin{aligned}
K_{(13)} &= S^2\gamma_4, \\
K_{(14)} &= T^2\gamma_4, \\
K_{(15)} &= K_{(16)} = K_{(17)} = ST\gamma_4.
\end{aligned} \tag{B3}
$$

Given the limited types of allowed deformations as in Eq. (2), we can estimate the biaxial elasticities based on the uniaxial moduli and scalar order parameters of chiral nematic systems (see Sec. VIII A).

TABLE III. Biaxial elastic moduli estimation for two biaxial systems, both derived from nematic 5CB, one doped with a chiral additive and the other with anisotropic nanoparticles to form a molecular-colloidal hybrid LC.

Elastic constants (pN)	Chiral nematic LC	Hybrid LC [44]
K_1	6	6.15
K_2	3	3
K_3	10	10
K_4	~0	~0
K_5	~0	~0
K_6	~0	0.3
K_7	0.007	6.45
K_8	~0	10
K_9	~0	6.15
$K_{(10)}$	0.005	~0
$K_{(11)}$	0.009	3
$K_{(12)}$	0.014	10.3

Taking a 5CB-dominated LC with a cholesteric pitch $p = 5$ μm, we estimated the 12 elastic moduli and compared them to another studied biaxial LC system (Table III) [44].

As one would expect, weaker biaxiality compared to hybrid systems implies weaker biaxial elasticities. Manufacturing technologies associated with cholesterics are, however, much more developed for exploring the biaxial topologies in D2CLC soft matter systems.

[1] N. D. Mermin, *The topological theory of defects in ordered media*, Rev. Mod. Phys. **51**, 591 (1979).

[2] M. Kléman, *Defects in liquid crystals*, Rep. Prog. Phys. **52**, 555 (1989).

[3] T. De'Neve, M. Kleman, and P. Navard, *Defect morphology in a biaxial thermotropic polymer*, J. Phys. II (France) **2**, 187 (1992).

[4] I. Ovidko and A. Romanov, *Topological excitations (defects, solitons, textures, frustrations) in condensed media*, Phys. Status Solidi (a) **104**, 13 (1987).

[5] D. R. Nelson, *Defects and Geometry in Condensed Matter Physics* (Cambridge University Press, Cambridge, England, 2002).

[6] N. Goldenfeld, *Dynamics of cosmological phase transitions: What can we learn from condensed matter physics?*, in *Formation and Interactions of Topological Defects: Proceedings of a NATO Advanced Study Institute on Formation and Interactions of Topological Defects* (Springer, Boston, 1995), pp. 93–104.

[7] T. W. B. Kibble, *Topology of cosmic domains and strings*, J. Phys. A **9**, 1387 (1976).

[8] T. W. B. Kibble, *Phase transitions in the early universe and defect formation*, in *Formation and Interactions of Topological Defects: Proceedings of a NATO Advanced Study*

Institute on Formation and Interactions of Topological Defects (Springer, Boston, 1995), pp. 1–26.
[9] M. Freiser, *Ordered states of a nematic liquid*, Phys. Rev. Lett. **24**, 1041 (1970).
[10] Q. Liu, P. J. Ackerman, T. C. Lubensky, and I. I. Smalyukh, *Biaxial ferromagnetic liquid crystal colloids*, Proc. Natl. Acad. Sci. U.S.A. **113**, 10479 (2016).
[11] H. Mundoor, J.-S. Wu, H. H. Wensink, and I. I. Smalyukh, *Thermally reconfigurable monoclinic nematic colloidal fluids*, Nature (London) **590**, 268 (2021).
[12] H. Mundoor, S. Park, B. Senyuk, H. H. Wensink, and I. I. Smalyukh, *Hybrid molecular-colloidal liquid crystals*, Science **360**, 768 (2018).
[13] I. I. Smalyukh, *Knots and other new topological effects in liquid crystals and colloids*, Rep. Prog. Phys. **83**, 106601 (2020).
[14] C. Tschierske and D. J. Photinos, *Biaxial nematic phases*, J. Mater. Chem. **20**, 4263 (2010).
[15] G. R. Luckhurst and T. J. Sluckin, *Biaxial Nematic Liquid Crystals: Theory, Simulation and Experiment* (John Wiley & Sons, New York, 2015).
[16] R. G. Priest and T. C. Lubensky, *Biaxial model of cholesteric liquid crystals*, Phys. Rev. A **9**, 893 (1974).
[17] J.-S. Wu, M. T. Lazaro, S. Ghosh, H. Mundoor, H. H. Wensink, and I. I. Smalyukh, *Unavoidable emergent biaxiality in chiral molecular-colloidal hybrid liquid crystals*, Phys. Rev. E **111**, 045410 (2025).
[18] J.-S. Wu, M. T. Lázaro, H. Mundoor, H. H. Wensink, and I. I. Smalyukh, *Emergent biaxiality in chiral hybrid liquid crystals*, Nat. Commun. **15**, 9941 (2024).
[19] G. Toulouse, *Pour les nématiques biaxes*, J. Phys. (Paris), Lett. **38**, 67 (1977).
[20] V. Poenaru and G. Toulouse, *The crossing of defects in ordered media and the topology of 3-manifolds*, J. Phys. (Paris) **38**, 887 (1977).
[21] G. P. Alexander and R. D. Kamien, *Entanglements and whitehead products: Generalizing Kleman's construction to higher-dimensional defects*, Liq. Cryst. Rev. **10**, 91 (2022).
[22] G. Q. AI *et al.*, *Non-Abelian braiding of graph vertices in a superconducting processor*, Nature (London) **618**, 264 (2023).
[23] M. Iqbal, N. Tantivasadakarn, R. Verresen, S. L. Campbell, J. M. Dreiling, C. Figgatt, J. P. Gaebler, J. Johansen, M. Mills, S. A. Moses *et al.*, *Non-Abelian topological order and anyons on a trapped-ion processor*, Nature (London) **626**, 505 (2024).
[24] C. Nayak, S. H. Simon, A. Stern, M. Freedman, and S. Das Sarma, *Non-Abelian anyons and topological quantum computation*, Rev. Mod. Phys. **80**, 1083 (2008).
[25] M. C. J. M. Vissenberg, S. Stallinga, and G. Vertogen, *Generalized Landau–de Gennes theory of uniaxial and biaxial nematic liquid crystals*, Phys. Rev. E **55**, 4367 (1997).
[26] E. Govers and G. Vertogen, *Elastic continuum theory of biaxial nematics*, Phys. Rev. A **30**, 1998 (1984).
[27] N. V. Priezjev and R. A. Pelcovits, *Coarsening dynamics of biaxial nematic liquid crystals*, Phys. Rev. E **66**, 051705 (2002).
[28] T. Lubensky, *Molecular description of nematic liquid crystals*, Phys. Rev. A **2**, 2497 (1970).
[29] L. Longa, D. Monselesan, and H.-R. Trebin, *An extension of the Landau-Ginzburg–de Gennes theory for liquid crystals*, Liq. Cryst. **2**, 769 (1987).
[30] D. A. Beller, T. Machon, S. Čopar, D. M. Sussman, G. P. Alexander, R. D. Kamien, and R. A. Mosna, *Geometry of the cholesteric phase*, Phys. Rev. X **4**, 031050 (2014).
[31] J.-S. Wu and I. I. Smalyukh, *Hopfions, heliknotons, skyrmions, torons and both Abelian and non-Abelian vortices in chiral liquid crystals*, Liq. Cryst. Rev. **10**, 34 (2022).
[32] Q. Zhang, P. J. Ackerman, Q. Liu, and I. I. Smalyukh, *Interactions of micro-rods in a thin layer of a nematic liquid crystal*, Phys. Rev. Lett. **115**, 097802 (2015).
[33] S. Čopar, M. R. Dennis, R. D. Kamien, and S. Žumer, *Singular values, nematic disclinations, and emergent biaxiality*, Phys. Rev. E **87**, 050504(R) (2013).
[34] Y. Nozaki, T. Kálmán, M. Teragaito, and Y. Koda, *Homotopy classification of knotted defects in ordered media*, Proc. R. Soc. A **480**, 20240148 (2024).
[35] H. Nakanishi, K. Hayashi, and H. Mori, *Topological classification of unknotted ring defects*, Commun. Math. Phys. **117**, 203 (1988).
[36] T. Annala, R. Zamora-Zamora, and M. Möttönen, *Topologically protected vortex knots and links*, Commun. Phys. **5**, 309 (2022).
[37] G. P. Alexander, Bryan Gin-gee Chen, E. A. Matsumoto, and R. D. Kamien, *Colloquium: Disclination loops, point defects, and all that in nematic liquid crystals*, Rev. Mod. Phys. **84**, 497 (2012).
[38] M. Kleman and O. D. Lavrentovich, *Soft Matter Physics: An Introduction* (Springer, New York, 2003).
[39] A. Hatcher, *Algebraic Topology* (Cambridge University Press, Cambridge, England, 2002).
[40] Note that Figs. 2(a) and 2(b) can be continuously interchanged by a local π rotation of each triad about the horizontal axis since they belong to the same conjugacy class. They are, however, topologically distinguishable as group elements by their winding numbers; they can morph one to the other by circumnavigating around a third defect, as shown in Fig. 3.
[41] G. E. Volovik and V. P. Mineev, *Investigation of singularities in superfluid* He^3 *in liquid crystals by the homotopic topology methods*, Sov. Phys. JETP **45**, 1186 (1977).
[42] L. Michel, *Symmetry defects and broken symmetry. Configurations hidden symmetry*, Rev. Mod. Phys. **52**, 617 (1980).
[43] J. Pollard and G. P. Alexander, *Contact topology and the classification of disclination lines in cholesteric liquid crystals*, Phys. Rev. Lett. **130**, 228102 (2023).
[44] B. Senyuk, H. Mundoor, I. I. Smalyukh, and H. H. Wensink, *Nematoelasticity of hybrid molecular-colloidal liquid crystals*, Phys. Rev. E **104**, 014703 (2021).
[45] E. F. Gramsbergen, L. Longa, and W. H. de Jeu, *Landau theory of the nematic-isotropic phase transition*, Phys. Rep. **135**, 195 (1986).
[46] D. Allender and L. Longa, *Landau–de Gennes theory of biaxial nematics reexamined*, Phys. Rev. E **78**, 011704 (2008).

[47] D. M. Sussman and D. A. Beller, *Fast, scalable, and interactive software for Landau–de Gennes numerical modeling of nematic topological defects*, Front. Phys. **7**, 204 (2019).
[48] P. J. Ackerman and I. I. Smalyukh, *Diversity of knot solitons in liquid crystals manifested by linking of preimages in torons and hopfions*, Phys. Rev. X **7**, 011006 (2017).
[49] M. Ravnik and S. Žumer, *Landau–de Gennes modelling of nematic liquid crystal colloids*, Liq. Cryst. **36**, 1201 (2009).
[50] D. Mucci and L. Nicolodi, *On the Landau–de Gennes elastic energy of constrained biaxial nematics*, SIAM J. Math. Anal. **48**, 1954 (2016).
[51] M. Kleman and J. Friedel, *Lignes de dislocation dans les cholestériques*, J. Phys. (Paris), Colloq. **30**, C4-43 (1969).
[52] E. Efrati and W. T. M. Irvine, *Orientation-dependent handedness and chiral design*, Phys. Rev. X **4**, 011003 (2014).
[53] C. Meng, J.-S. Wu, and I. I. Smalyukh, *Topological steering of light by nematic vortices and analogy to cosmic strings*, Nat. Mater. **22**, 64 (2023).
[54] V. Chigrinov, H. S. Kwok, H. Takada, and H. Takatsu, *Photo-aligning by azo-dyes: Physics and applications*, Liquid Crystals Today **14**, 1 (2005).
[55] J.-B. Fleury, D. Pires, and Y. Galerne, *Self-connected 3D architecture of microwires*, Phys. Rev. Lett. **103**, 267801 (2009).
[56] M. Wang, Y. Li, and H. Yokoyama, *Artificial web of disclination lines in nematic liquid crystals*, Nat. Commun. **8**, 388 (2017).
[57] I. Nys, *Patterned surface alignment to create complex three-dimensional nematic and chiral nematic liquid crystal structures*, Liquid Crystals Today **29**, 65 (2020).
[58] A. Martinez, H. C. Mireles, and I. I. Smalyukh, *Large-area optoelastic manipulation of colloidal particles in liquid crystals using photoresponsive molecular surface monolayers*, Proc. Natl. Acad. Sci. U.S.A. **108**, 20891 (2011).
[59] T. Lee, R. P. Trivedi, and I. I. Smalyukh, *Multimodal nonlinear optical polarizing microscopy of long-range molecular order in liquid crystals*, Opt. Lett. **35**, 3447 (2010).
[60] I. I. Smalyukh and O. D. Lavrentovich, *Three-dimensional director structures of defects in Grandjean-Cano wedges of cholesteric liquid crystals studied by fluorescence confocal polarizing microscopy*, Phys. Rev. E **66**, 051703 (2002).
[61] H. Mori, E. C. Gartland, Jr., J. R. Kelly, and P. J. Bos, *Multidimensional director modeling using the q tensor representation in a liquid crystal cell and its application to the π cell with patterned electrodes*, Jpn. J. Appl. Phys. **38**, 135 (1999).
[62] A. B. Harris, R. D. Kamien, and T. C. Lubensky, *Microscopic origin of cholesteric pitch*, Phys. Rev. Lett. **78**, 1476 (1997).
[63] T. Kroin, A. M. Figueiredo Neto, L. Liébert, and Y. Galerne, *Chirality-induced biaxiality at the uniaxial-to-biaxial cholesteric phase transition*, Phys. Rev. A **40**, 4647 (1989).
[64] L. Longa, W. Fink, and H.-R. Trebin, *Biaxiality of chiral liquid crystals*, Phys. Rev. E **50**, 3841 (1994).
[65] M. I. Monastyrskiĭ and P. V. Sasorov, *Bound states of linear defects in biaxial nematics and superfluid liquids*, J. Exp. Theor. Phys. **102**, 149 (2006).
[66] D. S. Hall, M. W. Ray, K. Tiurev, E. Ruokokoski, A. H. Gheorghe, and M. Möttönen, *Tying quantum knots*, Nat. Phys. **12**, 478 (2016).
[67] H. Rajamäki, T. Annala, and M. Möttönen, *Topologically protected vortex knots in an experimentally realizable system*, Phys. Rev. Lett. **133**, 236604 (2024).
[68] M. Kobayashi, *Physics of non-Abelian vortices in Bose-Einstein condensates*, J. Phys. Conf. Ser. **297**, 012013 (2011).
[69] I. Nys, M. Stebryte, Y. Y. Ussembayev, J. Beeckman, and K. Neyts, *Tilted chiral liquid crystal gratings for efficient large-angle diffraction*, Adv. Opt. Mater. **7**, 1901364 (2019).
[70] J.-S. B. Tai, J.-S. Wu, and I. I. Smalyukh, *Geometric transformation and three-dimensional hopping of Hopf solitons*, Nat. Commun. **13**, 2986 (2022).
[71] C. Meng, J.-S. Wu, Žiga Kos, J. Dunkel, C. Nisoli, and I. I. Smalyukh, *Emergent dimer-model topological order and quasi-particle excitations in liquid crystals: Combinatorial vortex lattices*, arXiv:2502.08314 [Phys. Rev. X (to be published)].